

Article

Impact of Radar and Surface Data Assimilation on the Forecast of a Nocturnal Squall Line in the Yangtze–Huaihe River

Zongmei Pan , Shuwen Zhang *  and Weidong Zhang

Key Laboratory of Climate Resource Development and Disaster Prevention in Gansu Province,
College of Atmospheric Sciences, Lanzhou University, Lanzhou 730000, China

* Correspondence: zhangsw@lzu.edu.cn

Abstract: The impact of radar and surface data assimilation on the forecast of a nocturnal squall line initiated above the stable boundary layer in the Yangtze–Huaihe River is investigated by the Weather Research and Forecasting (WRF) model and its three-dimensional variational assimilation system (WRFDA 3DVar). Results show that the assimilation of radar and surface data can improve the prediction of the convection initiation time, height and vertical ascending motion during the early stage of the squall line formation by adjusting the thermodynamic structure, circulation patterns, water vapor conditions and hydrometeor mixing ratios. Although the radar and surface data assimilation can improve the forecast of the location of the squall line to a certain extent, the squall line is stronger in the radar data assimilation than that in the surface data assimilation, leading to stronger radar reflectivity and heavier precipitation. The assimilation of both radar and surface data has a more positive impact on the forecast skill than the assimilation of either type of data. Moreover, during the mature stage of the squall line, radar and surface data assimilation can enhance the intensity of the surface cold pool. Specifically, radar data assimilation or assimilating the two data simultaneously can produce a stronger cold pool than only assimilating surface data, which is more conducive to the maintenance and development of the squall line.

Keywords: data assimilation; nocturnal squall line; stable boundary layer; convection initiation; cold pool



Citation: Pan, Z.; Zhang, S.; Zhang, W. Impact of Radar and Surface Data Assimilation on the Forecast of a Nocturnal Squall Line in the Yangtze–Huaihe River. *Atmosphere* **2022**, *13*, 1522. <https://doi.org/10.3390/atmos13091522>

Academic Editor: Meelis Zidikheri

Received: 31 July 2022

Accepted: 30 August 2022

Published: 17 September 2022

Publisher's Note: MDPI stays neutral with regard to jurisdictional claims in published maps and institutional affiliations.



Copyright: © 2022 by the authors. Licensee MDPI, Basel, Switzerland. This article is an open access article distributed under the terms and conditions of the Creative Commons Attribution (CC BY) license (<https://creativecommons.org/licenses/by/4.0/>).

1. Introduction

Squall lines are mesoscale convective systems (MCSs), which are banded thunderstorms developed under the interaction of large-scale environmental and mesoscale conditions [1]. The horizontal scale of squall lines is usually tens to hundreds of kilometers long and tens of kilometers wide. Squall lines may produce heavy rainfall, thunderstorms and gales, hail, tornadoes and other disastrous weather, all of which seriously impact human life [2].

With the continuous improvement in mesoscale numerical models, great progress has been made in predicting squall lines. However, the initial conditions of the mesoscale numerical models mainly come from the background fields provided by the large-scale models. Due to the limitation of temporal and spatial resolution, these data provide little meso- and micro-scale information about the initial conditions of the models. Thus, it is challenging to predict squall lines accurately [3]. The Doppler weather radar can provide detailed data to detect the internal structure and evolution characteristics of squall lines. Assimilation of the radar data into mesoscale numerical models can provide more accurate and reliable initial conditions, making the forecast of squall lines more precise and effective. At present, many studies have analyzed the impact of the radar data assimilation on the forecast of squall lines, indicating that radar data assimilation can adjust the environmental fields such as the low-level and upper-level wind field, the distribution of hydrometeors, humidity and divergence, thereby improving the prediction

of squall lines intensity, location, duration and so on [4–8]. Although the radar can provide high spatial–temporal resolution data, it usually cannot detect near-surface data due to the influence of detection range, terrain occlusion, earth curvature and the spatial resolution of the pixels in front of the punctual ground registers. When the squall line is more than 100 km away from the radar station, the radar can only detect data over 2 km above the altitude of the radar station [9]. However, the initiation of squall lines is particularly sensitive to the thermal and humidity changes in the atmospheric boundary layer. The cold pool and low-level wind shear are two critical factors for the development and maintenance of squall lines; thus, an appropriate initial state of the lower atmosphere is necessary for squall lines prediction. To fill the detection defect of the radar in the near-surface layer, some studies have assimilated the surface data into the storm scale forecast system, and it has been shown that assimilating the surface data can improve the meteorological conditions near the surface, and thus improve the forecast of heavy rainfall [9,10].

The above studies show the impact of radar and surface data assimilation on the forecast of squall lines, but most of these studies focus on squall lines that occur during the daytime, and there are few studies on nocturnal squall lines. The convection initiation during the daytime is mostly surface based, and its initiation and development are mostly related to the convergence lines (dry lines, storm outflows, sea wind fronts, etc.) in the convective boundary layer [11]. However, the convective thermal environment and dynamic forcing mechanism at night are quite different from those during the daytime, and most of them are related to low-level jets [12,13], gravity waves [14,15], bores and density currents [16,17]. Moreover, the stable boundary layer at night will inhibit the convergence on the surface, and thus convections at night are generally initiated above the boundary layer [18,19]. Because of the lack of high-spatial and temporal resolution observations in the boundary layer, the prediction of nocturnal convection will be difficult. Thus, it is essential to assimilate both radar and surface observation data to improve the prediction of nocturnal squall lines [20].

This study selects a nocturnal squall line in the Yangtze–Huaihe River. It focuses on the following two issues: When the squall line is initiated above the stable boundary layer, can the assimilation of radar and surface observation data improve the forecast of the nocturnal squall line? If so, what is the impact of the assimilation of each kind of observation, respectively, and how do they interact? This study is organized as follows: Section 1 is the introduction. Section 2 (data and methods) introduces the observation data, assimilation method, model configuration and experimental design and the verification method. Section 3 briefly introduces the nocturnal squall line. Results are verified and analyzed in Section 4. Discussion and conclusions are provided in Section 5.

2. Data and Methods

2.1. Observation Data

All observations used in this study are provided by the “Observation, Prediction and Analysis of severe Convection of China” (OPACC) project [21].

2.1.1. Radar Observation Data

The radar observation data used in this study are 9 Doppler weather radars from the China Next Generation Weather Radar (CINRAD), including Zhumadian (ZMD; 114.020° E, 33.010° N; 189.1 m), Nanyang (NY; 112.493° E, 33.021° N; 231.4 m), Suizhou (SZ; 113.389° E, 31.726° N; 136 m), Fuyang (FY; 115.741° E, 32.879° N; 66.2 m), Hefei (HF; 117.258° E, 31.867° N; 165.6 m), Bengbu (BB; 117.448° E, 32.918° N; 149.6 m), Zhengzhou (ZZ; 113.697° E, 34.704° N; 202 m), Wuhan (WH; 114.378° E, 30.517° N; 135.7 m) and Yichang (YC; 111.296° E, 30.702° N; 203.8 m) stations. The distribution of radar observation stations is shown by the big blue spots in Figure 1. The radars use volume cover pattern 21 (VCP21) observation mode for continuous volume scans, with the elevation progressively increasing from 0.5° to 19.5°, and provide the observations of reflectivity, radial velocity and spectrum width. The reflectivity values are recorded at 1 km intervals along the radar beam, and the

radial velocity values are recorded at 250 m intervals. The maximum detection radius of the radar is 460 km, and the frequency of radar data is approximated to 6 min.

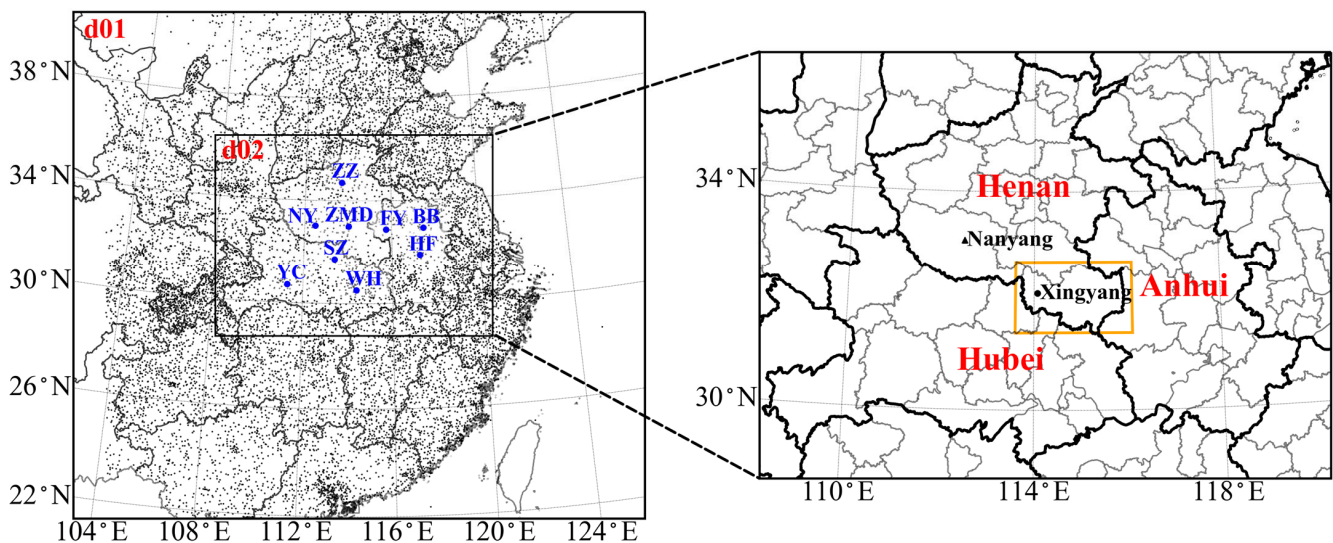


Figure 1. Model domain, distribution of radar and surface observation stations, the geographic information of the area of interest and other geographic conditions. The big blue spots represent the locations of the radar stations from Zhumadian (ZMD), Nanyang (NY), Suizhou (SZ), Fuyang (FY), Hefei (HF), Bengbu (BB), Zhengzhou (ZZ), Wuhan (WH), Yichang (YC). The small black spots represent the locations of surface data stations in the left panel. The orange box represents the area of interest, the black dot represents the location of Xinyang City, Henan Province, and the black triangle represents the location of the Nanyang Sounding Station in the right panel.

Prior to data assimilation, the quality of the radar observation data is strictly controlled, including eliminating ground clutter, removing reflectivity generated by the interference of the same wavelength, removing isolated points for reflectivity and radial velocity, correcting radial velocity based on spectrum width threshold and dealiasing radial velocity through the region-based method available in the Python-ARM Radar Toolkit (Py-ART) [22]. In addition, radar observation data are thinned to the model grid after quality control. Based on previous research work [23–25], the radar reflectivity observation error is set to 2 dBZ, and the radial velocity observation error is set to 1 m/s.

2.1.2. Surface Observation Data

The surface observation data are from over 10,000 Automatic Weather Stations (AWS) observations in China, which have undergone extreme value checks, temporal and spatial consistency checks, etc. during the collection process. The time interval for the AWS data is 10 min. The AWS data include 24 variables, such as sea-level pressure, 2 m temperature, 2 m dew point temperature, 3 h pressure change, 6 h precipitation, 10 m wind speed and wind direction.

The AWS data have been preprocessed through the observation preprocessing program (OBSPROC) included in the WRF Variational Data Assimilation (WRFDA) package before assimilation. The OBSPROC can remove the observations out of the model domain, discard duplicate observations, assign observation errors and perform some quality control checks. The locations of the AWS data after OBSPROC preprocessing are shown in Figure 1 (small black spot).

2.1.3. Sounding and Precipitation Observation Data

The sounding data used in this study are the observations of the upper-air meteorological observation stations in China. The sounding observations include data at 0000 UTC and

1200 UTC a day. The variables contained in the sounding data include geopotential height, temperature, dew point temperature, wind speed and wind direction. The precipitation observation data are the hourly precipitation observations from national automatic rainfall stations. The precipitation observation data are also checked by threshold value, temporal and spatial consistency.

2.2. Assimilation Method

2.2.1. Data Assimilation System

The data assimilation system is WRFDA 3DVar (V4.3.1), whose objective function is [26]:

$$J(\mathbf{x}) = \frac{1}{2}(\mathbf{x} - \mathbf{x}_b)^T \mathbf{B}^{-1}(\mathbf{x} - \mathbf{x}_b) + \frac{1}{2}[H(\mathbf{x}) - \mathbf{y}^o]^T \mathbf{R}^{-1}[H(\mathbf{x}) - \mathbf{y}^o] \quad (1)$$

where \mathbf{x} is the analysis state vector, \mathbf{x}_b is the background state vector, \mathbf{y}^o is the observation vector, H is the observation operator, \mathbf{B} is the background error covariance matrix and \mathbf{R} is the observation error covariance matrix. When the objective function takes a minimum value—that is, when $\nabla J(\mathbf{x}) = 0$ —the optimal estimate of the atmosphere state is obtained.

The background error covariance used in this study is estimated using the National Meteorological Center (NMC) method [27], which is implemented by taking the differences between the forecasts of different lengths valid (24 h forecast and 12 h forecast) at the same time over a 1-month period (from 10 June to 10 July 2014). In the process of estimating the background error covariance, model variables need to be transformed into a set of control variables. The control variable scheme used in this study is the CV5 scheme in WRFDA 3DVar, including the control variables of stream function (ψ), unbalanced velocity potential (χ_u), unbalanced temperature (T_u), pseudo relative humidity ($RH_{s,u}$) and unbalanced surface pressure ($P_{s,u}$) [28–30].

2.2.2. Radar Data Assimilation Scheme

The observations of reflectivity are directly assimilated based on the empirical relationship between the radar reflectivity and rainwater mixing ratio under the constraints of the warm rain scheme. The total water is used as the control variable, and the warm rain scheme is used to assist the calculation of hydrometeors. The observation operator for the radar reflectivity is [31]:

$$Z = 43.1 + 17.5 \log(\rho q_r) \quad (2)$$

where Z is the reflectivity in the unit of dBZ, ρ is the density of air, and q_r is the rainwater mixing ratio.

The observation operator for the radar radial velocity is calculated based on the wind field as [32]:

$$V_r = u \frac{x - x_i}{r_i} + v \frac{y - y_i}{r_i} + (w - v_T) \frac{z - z_i}{r_i} \quad (3)$$

where (u, v, w) is the three-dimensional wind field, (x, y, z) is the radar location, (x_i, y_i, z_i) is the location of the radar observation, r_i is the distance between the radar and the radar observation and v_T is the terminal velocity.

2.2.3. Surface Data Assimilation Scheme

The surface data assimilation scheme proposed by Ruggiero (1996) is used to deal with the terrain height [33]. The surface observation data are assimilated based on the lowest model level in the first guess. Surface data are not used when the height difference of the elevation of the observing site and the lowest model level height is larger than 100 m. The assimilated surface data include 2 m temperature, 2 m dew point temperature, 10 m wind, sea level pressure, 10 m wind speed and direction.

2.3. Model Configuration and Experimental Design

The Weather Research and Forecasting (WRF, V4.3.1) model is used in this study. The initial and boundary conditions of the model are provided by the $1^\circ \times 1^\circ$ FNL analysis

data with a 6 h interval from the National Centers for Environment Prediction (NCEP). Two nested domains with a horizontal resolution of 9 and 3 km are set for the model (Figure 1). The domains have 45 vertical layers with the model top at 50 hPa. The physical parameterization schemes of the numerical experiment include the Yonsei State University (YSU) boundary layer scheme [34], the WRF Double-Moment 6-class (WDM6) Microphysics scheme [35], the rapid radiative transfer model (RRTM) long-wave radiation scheme [36], the Dudhia short wave radiation scheme [37], the Noah land surface model land surface scheme [38] and the Kain–Fritsch cumulus scheme [39] for the 9 km domain (no cumulus parameterization scheme is used for 3 km domain). Two-way nesting is used in the model.

In order to explore the impact of radar and surface data assimilation on the forecast of this nocturnal squall line, four experiments are designed (Figure 2). The first experiment (noDA experiment) is a control experiment with no data assimilation, the second experiment (radarDA experiment) only assimilates the radar data, the third experiment (surfaceDA experiment) only assimilates the surface data and the fourth experiment (bothDA experiment) assimilates both the radar data and surface data simultaneously. Among them, the noDA experiment makes a 24 h forecast from 0000 UTC 11 July to 0000 UTC 12 July 2014, while in the radarDA, surfaceDA, and both DA experiments, the model is integrated from 0000 UTC to 1200 UTC 11 July, and then the observation data are assimilated every 30 min from 1200 UTC to 1500 UTC. The analysis field at 1500 UTC is used as the initial forecast field, and finally, the deterministic forecast is made for 9 h to 0000 UTC 12 July.

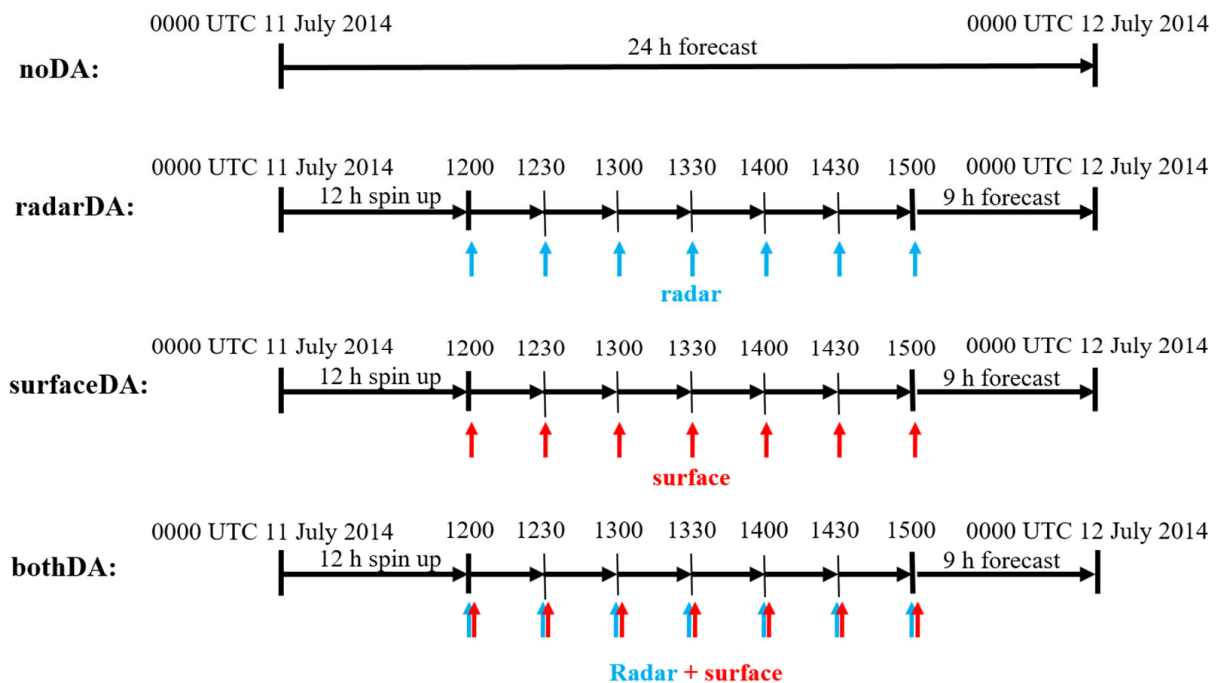


Figure 2. Flowchart for noDA, radarDA, surfaceDA and bothDA experiments.

2.4. Verification Method

The fractions skill score (FSS) is used to assess reflectivity forecast performance quantitatively. The fractions skill score is defined as:

$$FSS = 1 - \frac{\frac{1}{n} \sum_{i=1}^n (P_{fcst} - P_{obs})^2}{\frac{1}{n} \sum_{i=1}^n P_{fcst}^2 + \frac{1}{n} \sum_{i=1}^n P_{obs}^2} \tag{4}$$

where P_{fcst} and P_{obs} denote forecast and observed fractions of each grid when the forecast or observation is larger than a given threshold value and n is the number of grid points

where the observation exceeds the threshold. The range of *FSS* is 0–1 and its larger value indicates more excellent forecast skill.

The success ratio (*SR*), probability of detection (*POD*), bias score (*BIAS*) and threat score (*TS*) are used to evaluate the precipitation forecast. They are defined by the following formulation:

$$SR = \frac{A}{A + B} \quad (5)$$

$$POD = \frac{A}{A + C} \quad (6)$$

$$BIAS = \frac{A + B}{A + C} \quad (7)$$

$$TS = \frac{A}{A + B + C} \quad (8)$$

where *A*, *B* and *C* denote hits, false alarms and misses, respectively. The hits, false alarms and misses are defined by the categorical contingency table (Table 1).

Table 1. The categorical contingency table.

		Observation	
		Yes	No
Forecast	Yes	Hits	False alarms
	No	Misses	Correct rejections

The *SR*, *POD*, and *TS* range from 0 to 1. The higher the value of *SR*, *POD*, and *TS*, the greater the forecast skill. The range of *BIAS* is 0–∞. The ideal value of *BIAS* is one. When the value of *BIAS* is greater (less) than one, the predicted precipitation occurs more (less) than the observed precipitation.

We also use the root mean square error (*RMSE*) to assess the surface temperature forecast performance quantitatively:

$$RMSE = \sqrt{\frac{1}{N} \sum_{i=1}^N (T_i - O_i)^2} \quad (9)$$

where T_i is the forecast result, O_i is the observation and N is the total number of latitude and longitude grid points in the scoring area.

3. Case Overview

The nocturnal squall line occurred on the Meiyu front in Yangtze–Huaihe River from the night of 11 July to the morning of 12 July 2014. The area where the squall line formed and evolved is shown in the orange box in Figure 1.

3.1. Radar Reflectivity

As shown in the mosaics of radar composite reflectivity (Figure 3), stratiform cloud echoes existed in northwestern Henan and northern Hubei province during the daytime 11 July (Figure 3a). By night (1330 UTC), sporadic convection cells were generated near the border between Hubei and Henan, but their life history was short and dissipated quickly as they moved eastward (Figure 3b). A linear convection system was initiated at around 1530 UTC in the west of Xinyang city in Henan province (Figure 3c). Then, the linear convection system intensified as it moved eastward and developed into a squall line at 1700 UTC (Figure 3d). Subsequently, the squall line continued to strengthen (Figure 3e), and new convection cells were constantly being initiated at the south of the squall line, keeping the squall line in the south of Henan province (Figure 3f–h). Finally, the squall line began to dissipate at 2200 UTC.

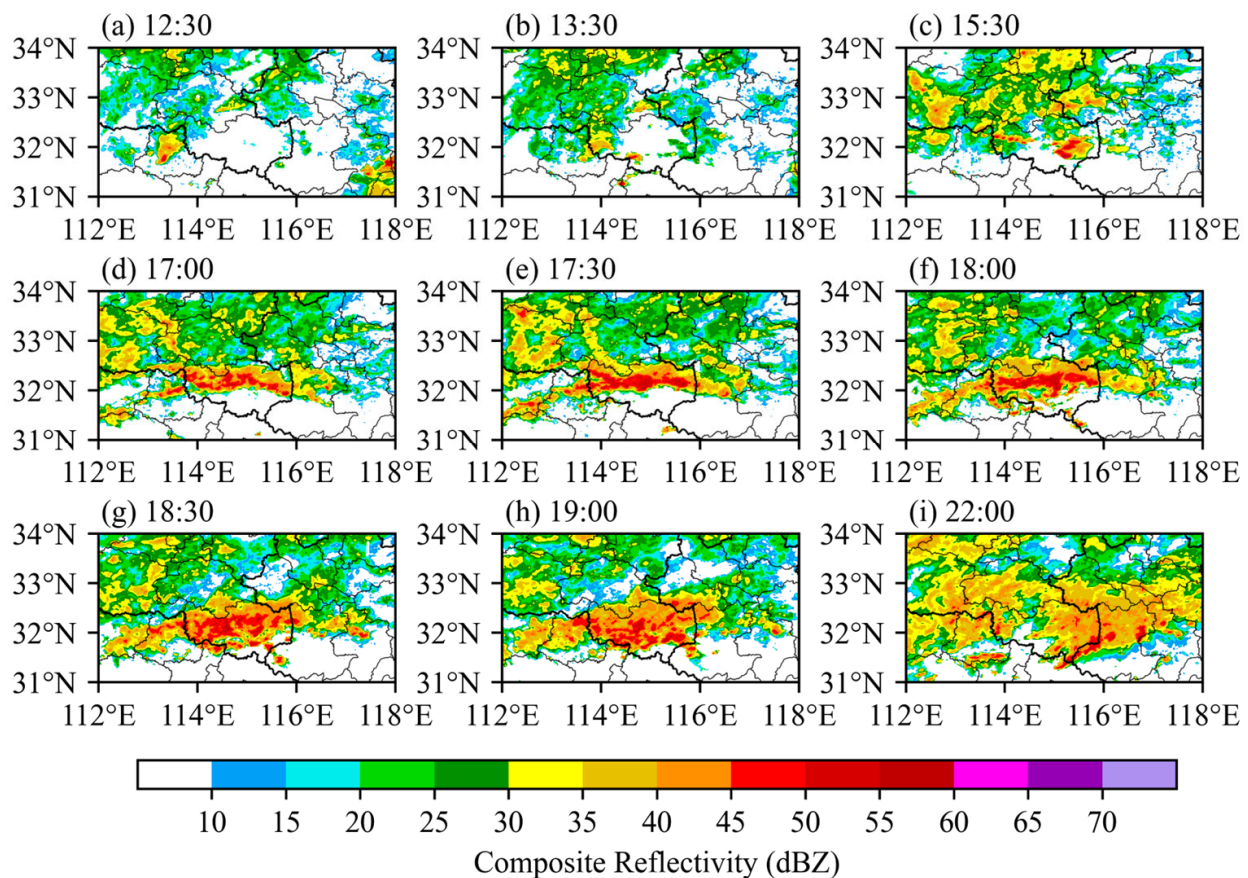


Figure 3. The mosaics of radar composite reflectivity (shaded, units: dBZ) at (a) 1230, (b) 1330, (c) 1530, (d) 1700, (e) 1730, (f) 1800, (g) 1830, (h) 1900, (i) 2200 UTC 11 July 2014.

3.2. Environmental Conditions

Figure 4 shows the environmental conditions before the squall line initiated at 1200 UTC 11 July. As can be seen from Figure 4a at 500 hPa, there was a vortex in northeast China. A low trough was formed in the Sichuan Basin. The subtropical high extended westward to around 110° E. At 850 hPa in Figure 4b, there was a low-level shear line in the Yangtze–Huaihe River, and a southwest vortex on the west side of the shear line. The warm and humid southwesterly wind converged with the dry and cold northerly wind at the junction of Henan, Hubei and Anhui. The convergence zone was located on the Meiyu front (Figure 4b). Thus, the environmental conditions were favorable for the convection initiation.

It is worth noting that the convective available potential energy (CAPE) at Nanyang station, which is closest to the region where the squall line formed, was $0 \text{ J}\cdot\text{kg}^{-1}$, and there was a certain temperature inversion below 880 hPa (Figure 4c). There was a layer of cold air near the surface. Thus, it was difficult for an air parcel lifted from the surface to pass through the inversion layer and obtain buoyancy. Therefore, this nocturnal squall line was initiated above the stable boundary layer, which is consistent with the result of He et al. (2018) [40].

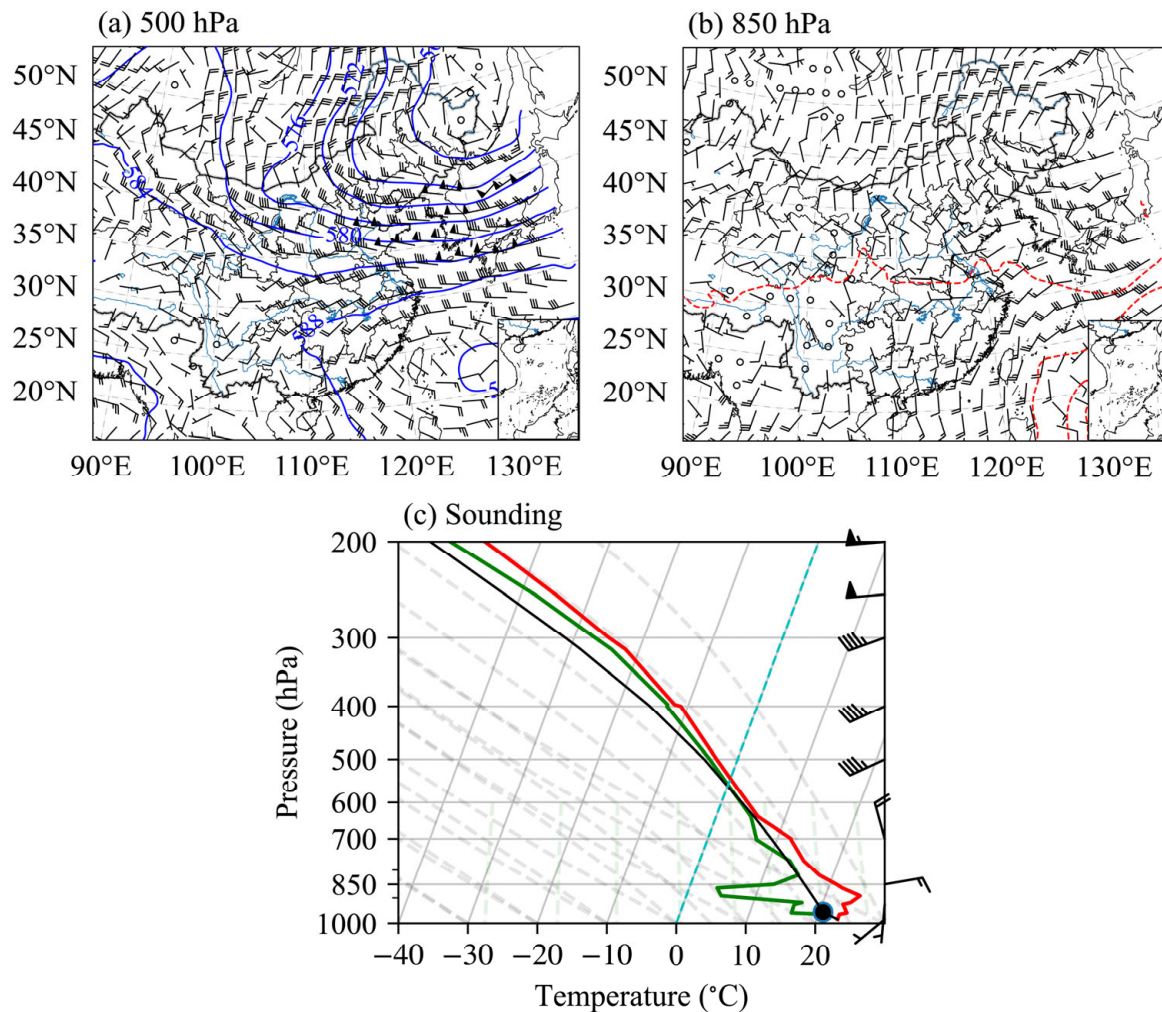


Figure 4. Weather charts from the fifth-generation ECMWF atmospheric reanalysis of the global climate (ERA5, $0.25^\circ \times 0.25^\circ$) data and the sounding chart from observation at 1200 UTC 11 July 2014, (a) 500 hPa and (b) 850 hPa geopotential height (blue solid lines, units: dagpm) and wind field (barbs, units: m/s), the red dashed line was the potential temperature of 345 K which indicated the location of MeiYu front in (b). (c) The sounding chart was taken at Nanyang station. The green line represents the dew point temperature profile, the black line represents the lifting curve, the red line represents the temperature profile and the black represents the lifting condensation level in (c). The location of Nanyang station is shown in Figure 1.

4. Results

4.1. Impact on the Forecast of the Squall Line

4.1.1. Radar Reflectivity

The radar composite reflectivity shows that, during the early stage of the squall line at 1530 UTC 11 July, there are multiple convection cells with reflectivity higher than 35 dBZ in the west of Xinyang city, Henan province, which are distributed in a northwest–southeast band (Figure 5a). In the noDA experiment (Figure 5b), although some convection cells are initiated at the border of Henan and Hubei, the intensity of convection is relatively weak, and the distribution is more dispersed with the position further south. In the radarDA experiment (Figure 5c), a linear convective system appears in southwest Henan province, which is stronger than the observed one, but some spurious convective cells are also initiated on the south side of the linear convective system. In the surfaceDA experiment (Figure 5d), there is also a linear convection system, whose location is closer to the observation but its intensity is relatively weak. In the bothDA experiment, the intensity

and location of the linear convective system are between the radarDA and surfaceDA experiment, but are closer to the observations (Figure 5e).

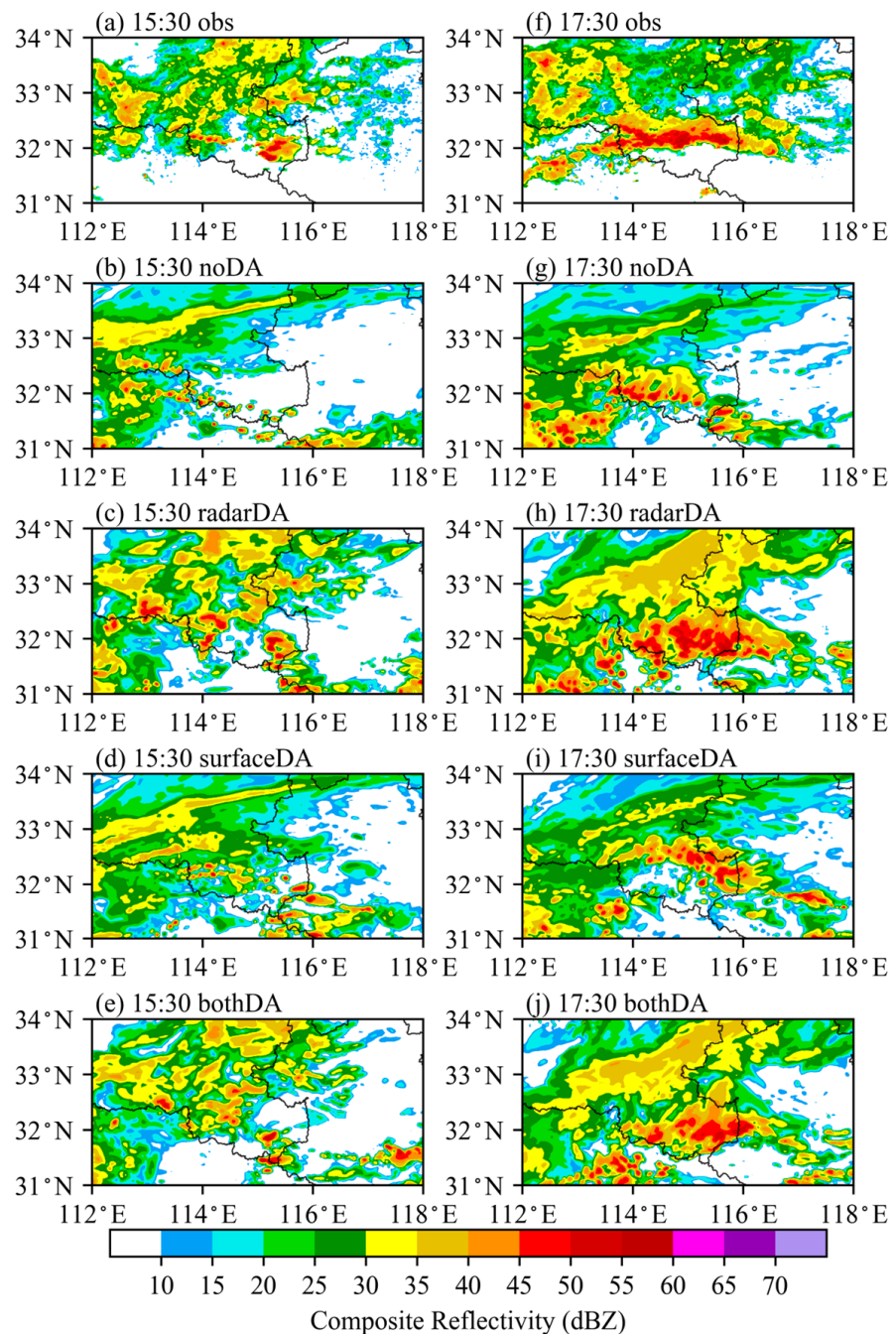


Figure 5. Radar composite reflectivity (shaded, units: dBZ) at (a–e) 1530 UTC and (f–i) 1730 UTC 11 July 2014 from the (a,f) observation, (b,g) noDA, (c,h) radarDA, (d,i) surfaceDA and (e,j) bothDA experiments.

In the mature stage of the squall line, it spans the southern part of Henan province in a west–east direction, and the composite reflectivity intensity exceeds 55dBZ (Figure 5f). In the noDA experiment, the intensity of the squall line is weaker and its location is further south than the observations with a north–west south–east direction (Figure 5g). In the radarDA experiment (Figure 5h), the shape, direction and position of the forecasted squall line are relatively closer to the observed. However, the radar reflectivity intensity is stronger and the coverage of strong echo is larger than the observations. In the surfaceDA experiment

(Figure 5i), the reflectivity intensity at the strong echo zone is closer to the observation and its position is shifted northward relative to the noDA experiment, but the squall line still remains in the northwest–southeast direction. In the bothDA experiment, the shape, direction and location of the squall line are similar to those in the radarDA experiment, but the intensity of the strong echo band is closer to the observations (Figure 5j).

It can be concluded that the radar or surface data assimilation can improve the forecast of the intensity and location of convection at the early stage of the squall line formation and its mature stage. To be specific, the radar data assimilation can change both the position and intensity of the convection, while the surface assimilation mainly affects the location of the convection. The best prediction is from the assimilation of both types of observation data.

Figure 6 shows the averaged fractions skill scores (FSS) of the radar composite reflectivity at different thresholds (10, 15, 20, 25, 30, 35, 40, 45, 50 dBZ) for noDA, radarDA, surfaceDA and bothDA experiments. The score area is consistent with the panel area in Figure 5. Overall, the three assimilation experiments have made better forecasts of radar reflectivity from 1500 to 1900 UTC than the noDA experiment. From the formation stage to the mature stage of the squall line (1530–1830 UTC), the improvement in radar reflectivity prediction in the bothDA experiment is greater than that in the radarDA and surfaceDA experiments. During the early stage of the squall line formation (1530–1630 UTC), the effect on the forecast of radar reflectivity in the radarDA experiment is slightly worse than that in the surfaceDA experiment, but it becomes better at a later time. The FSS of the surfaceDA experiment is slightly lower than that of the NoDA experiment at the mature stage of the squall line. This may be related to the weak reflectivity predicted by surfaceDA experiment.

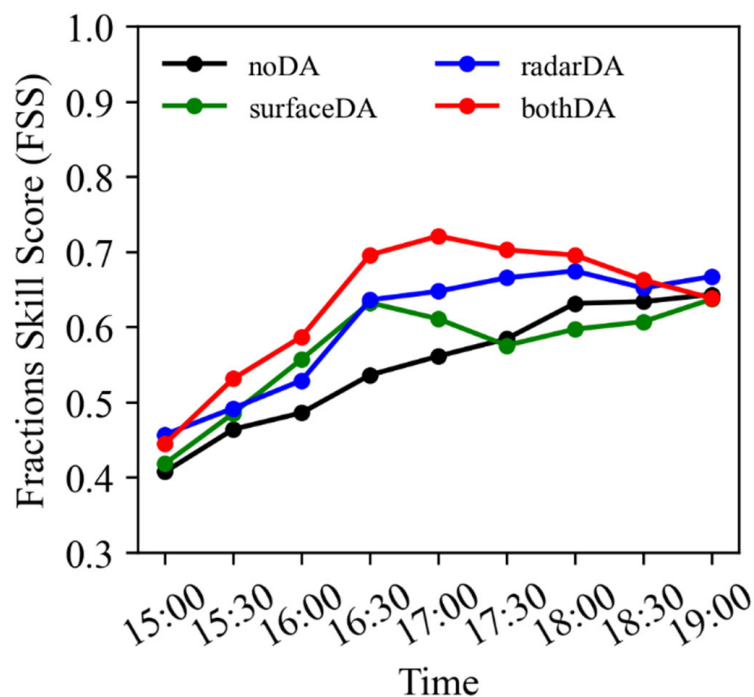


Figure 6. The averaged fractions skill scores (FSS) of the radar composite reflectivity at different thresholds (10, 15, 20, 25, 30, 35, 40, 45, 50 dBZ) from 1500 UTC to 1900 UTC 11 July 2014 for noDA (black dotted line), radarDA (blue dotted line), surfaceDA (green dotted line) and bothDA (red dotted line) experiments. The score area is the same as the panel area in Figure 5.

4.1.2. Precipitation

To further investigate the impact of assimilation on the squall line forecast, Figure 7 analyzes the accumulated precipitation for 6 h (1500–2100 UTC 11 July) from observations and four experiments. The four experiments are the same in the previous section. In the observation (Figure 7a), an east–west rain band with strong radar composite reflectivity

is located at the border of Henan, Hubei and Anhui. The center of heavy precipitation is in Xinyang city, Henan province, with the maximum precipitation exceeding 70 mm. The center of heavy precipitation predicted by the noDA experiment is southward, with strong spurious precipitation in the northern part of the Hubei province (Figure 7b). For the radarDA experiment, the intensity of heavy precipitation has been improved, but false or spurious precipitation appears at the border of the Henan and Anhui province, as well as the northeastern Hubei province (Figure 7c). The surfaceDA experiment reduces spurious precipitation and improves the precipitation fall zone effectively, but the intensity of precipitation is weak (Figure 7d). On the other hand, bothDA experiments can improve both the fall zone and intensity of precipitation and partly reduce spurious precipitation within the Hubei province (Figure 7e).

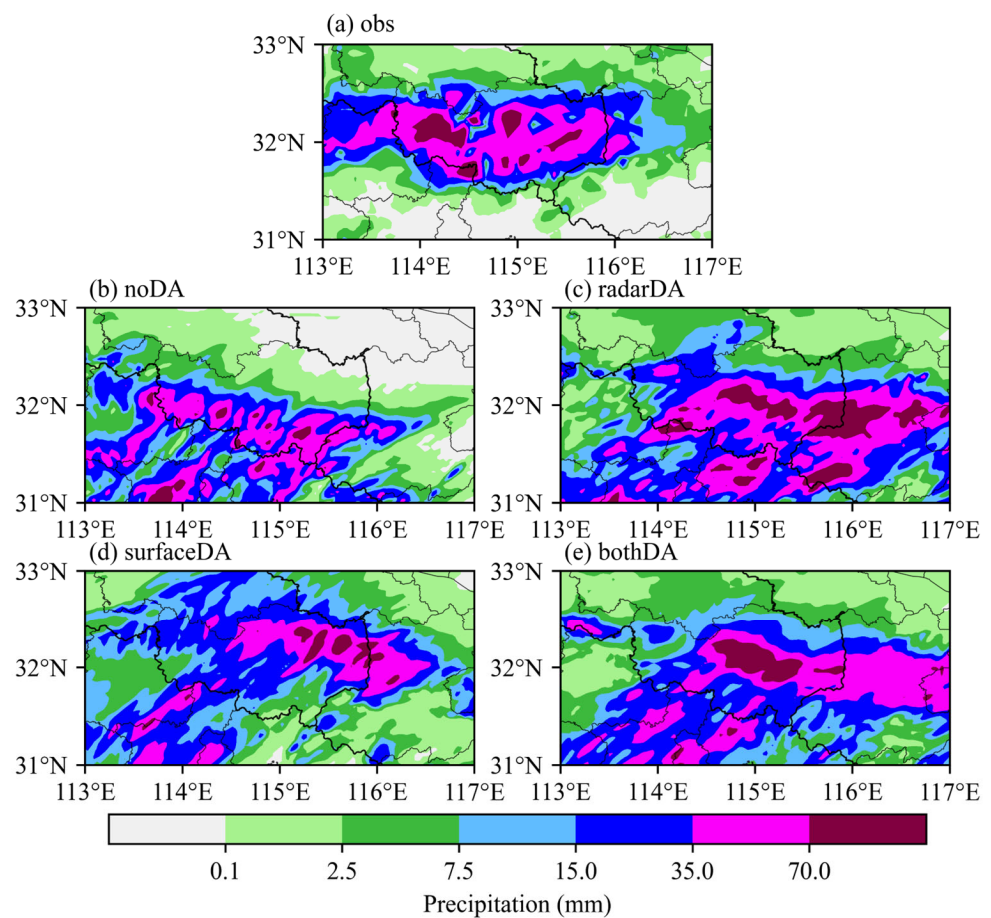


Figure 7. Distribution of 6h (1500 UTC to 2100 UTC 11 July 2014) accumulated precipitation (shaded, units: mm) from the (a) observation, (b) noDA, (c) radarDA, (d) surfaceDA and (e) bothDA experiments.

In conclusion, assimilating radar observation can increase the forecasted precipitation intensity, while assimilating surface observation can reduce the false precipitation forecasts and thus improve the precipitation fall zone. Assimilating both the radar and surface observations combines the advantages of the two kinds of observations and further enhances the best forecasts of precipitation intensity and fall zone.

In order to quantitatively evaluate the effect of the three assimilation experiments on the precipitation prediction, the performance diagram of 6 h (1500 to 2100 UTC 11 July 2014) accumulated precipitation for noDA, radarDA, surfaceDA and bothDA experiments is shown in Figure 8. The assimilation of radar and/or surface data positively contributes to the precipitation forecast. Specifically, for light precipitation threshold (≤ 15 mm), the prediction effect of accumulated precipitation in the surfaceDA experiment is the best, the

prediction effect in the radarDA experiment is relatively poor and the bothDA experiment is at a moderate level. As the precipitation magnitude increases, when the precipitation threshold is 35mm, the scores of the three assimilation experiments become close, and the radarDA experiment is the best. When the precipitation threshold is further increased to 70mm, the precipitation forecast in the bothDA experiment becomes the best. The forecast in the radarDA experiment is also better than that in the surfaceDA experiment.

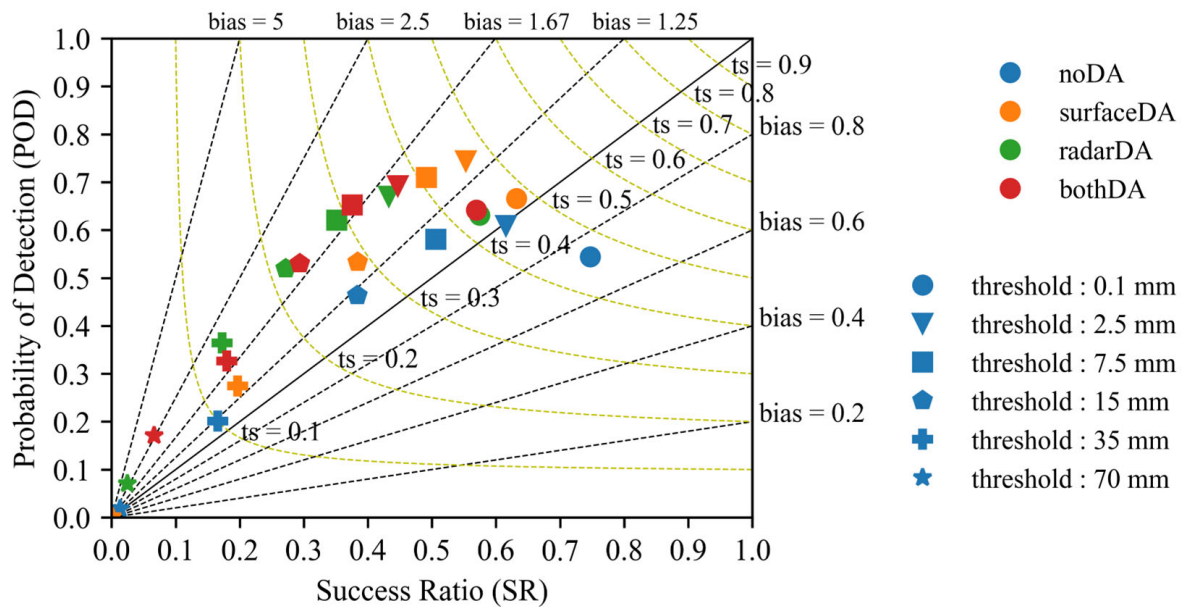


Figure 8. The performance diagram of 6 h (1500 UTC to 2100 UTC 11 July 2014) accumulated precipitation for noDA (blue markers), radarDA (green markers), surfaceDA (orange markers) and bothDA (red markers) experiments. The horizontal coordinates represent the success ratio (SR). The longitudinal coordinates represent the probability of detection (POD). Yellow curves represent the threat score (TS), and the black dashed lines represent the bias score (BIAS). The filled circle, down-pointing triangle, square, pentagon, plus and star makers represent different precipitation thresholds. The score area is the same as the panel area in Figure 7.

It can be seen that the assimilation of surface data has a better effect on the forecast of the light precipitation, which may be due to the improvement in the precipitation distribution as a result of assimilating the surface data. The radar data assimilation has a more obvious effect on the forecast of the heavy precipitation, because of the greater impact of radar data assimilation on the precipitation intensity. In addition, assimilating both radar and surface data can generate a good forecast of both light and heavy precipitation.

4.2. Impact on the Forecast of Convection Initiation of the Squall Line

4.2.1. Thermal Conditions

Since this squall line forms above the stable boundary layer at night, the thermodynamic structure is crucial to the forecast of the convection initiation. First, the surface temperature increments of the three assimilation experiments at 1300, 1400 and 1500 UTC are investigated. It can be seen from Figure 9 that the assimilation of radar data only reduces the surface temperature in parts areas of Henan, Anhui and Hubei from 1300 to 1500 UTC, and there is only a slight cooling in the west of Xinyang City at 1500 UTC. In the surfaceDA and bothDA experiments, the surface temperature almost decreases, with an obvious temperature drop at the junction of Henan and Hubei. Among them, the cooling range in the west of Xinyang in the bothDA experiment is more significant than that in the radarDA experiment. The effect of the three assimilation experiments on the surface temperature is further analyzed through the root mean square error (RMSE) of the surface temperature from 1200 to 1500 UTC. Figure 10 shows that the surface temperatures of the

three assimilation experiments are all closer to the observations than the noDA experiment. The bothDA experiment has generated the most significant improvement in surface temperature, the surfaceDA experiment is second, and the radarDA experiment is the smallest.

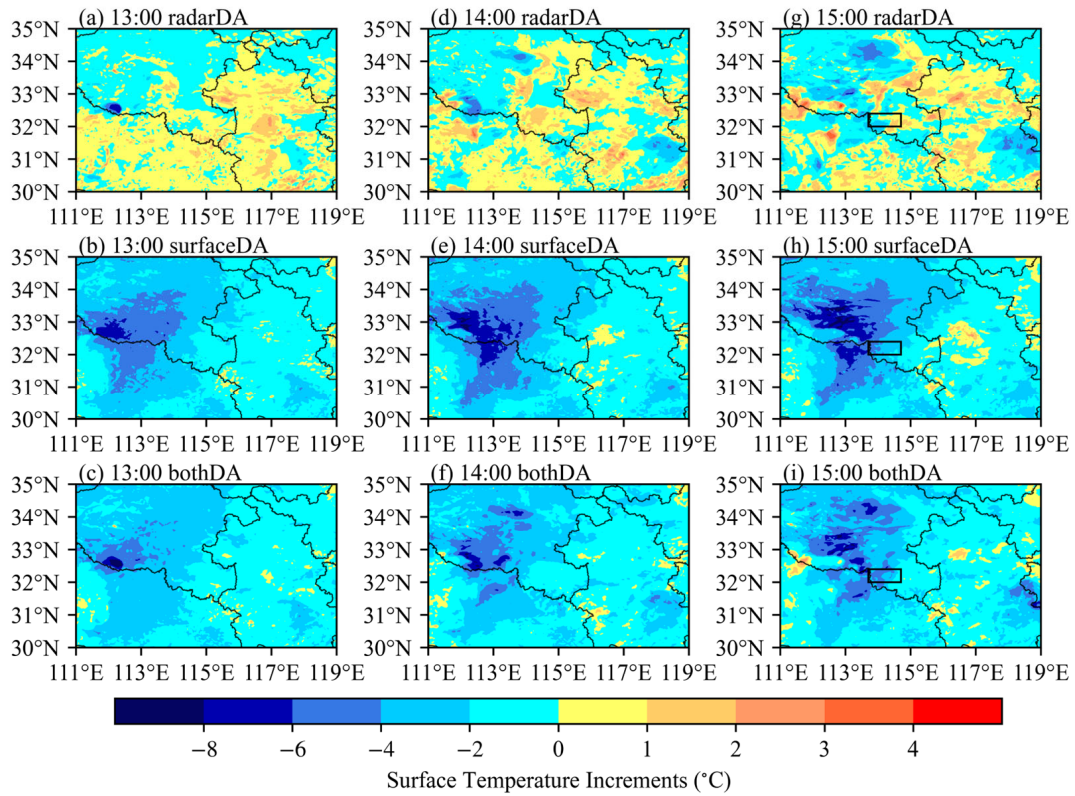


Figure 9. The surface temperature increments of the three assimilation experiments (shaded, unit: °C) at (a–c) 1300, (d–f) 1400 and (g–i) 1500 UTC 11 July 2014. The black box in (g–i) is where the squall line initiated.

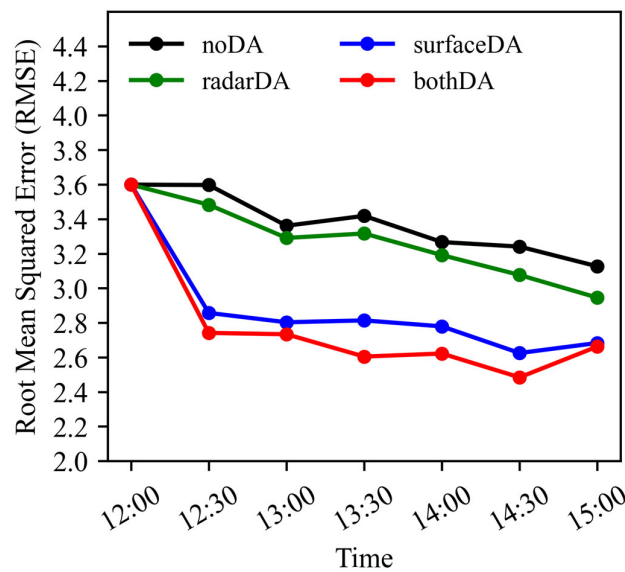


Figure 10. The Root Mean Squared Error (RMSE) for the surface temperature from 1200 to 1500 UTC 11 July 2014 for noDA (black dotted line), radarDA (green dotted line), surfaceDA (blue dotted line) and bothDA (red dotted line) experiments. The score area is the same as the panel area in Figure 9.

Then, we analyze the thermodynamic structure difference in the four experiments by comparing the soundings at 1530 UTC (Figure 11). The noDA experiment has high temperatures at the bottom of the boundary layer ($\sim 30^\circ\text{C}$). There is a surface temperature inversion, but a sharp temperature drop appears in 960 hPa–800 hPa, and the overall thermal environment in the boundary layer is relatively unstable. For the radarDA experiment, the surface temperature decreases to about 25°C , and the temperature within the boundary layer decreases slowly with the increase in height. Thus, its thermal environment is more stable than that in the noDA experiment. Moreover, the near-surface temperature is about 24°C with less variation in the height at the low levels in the surfaceDA experiment; the boundary layer has a more stable thermal environment than the radarDA experiment. The bothDA experiment has the lowest near-surface temperature ($\sim 23^\circ\text{C}$), and there is temperature inversion within the boundary layer. Thus, it has the most stable thermal environment.

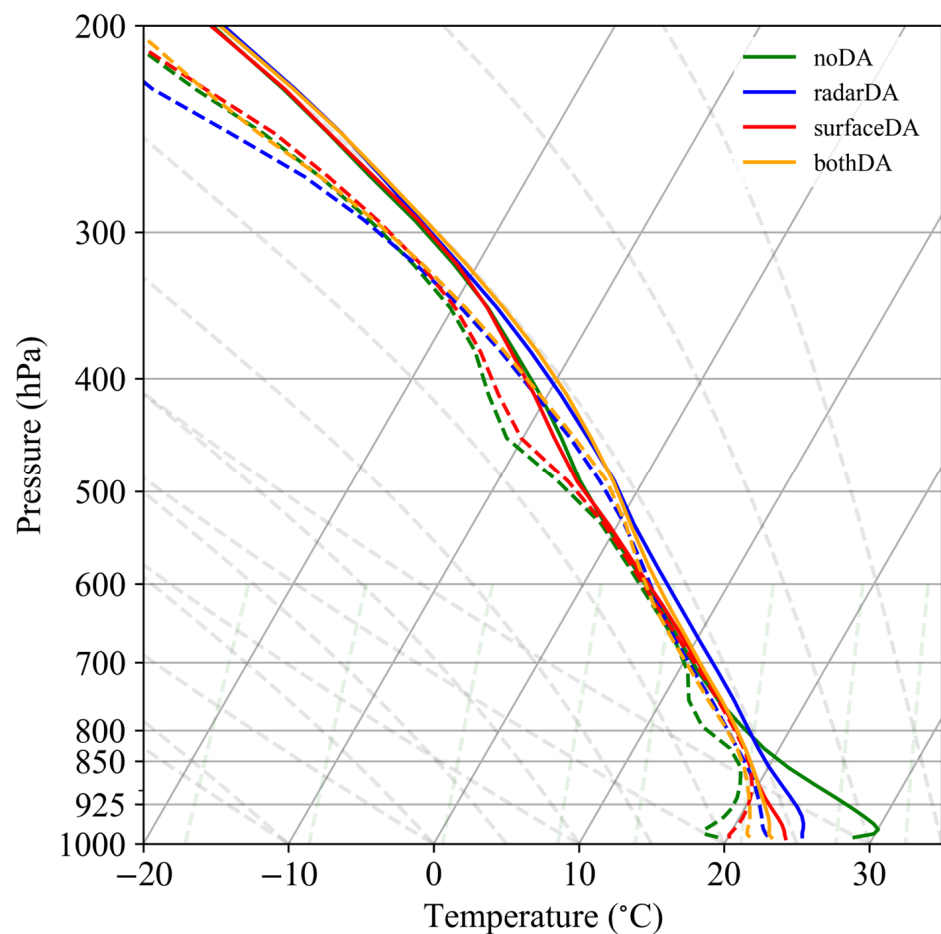


Figure 11. The area-averaged soundings taken in the initiation area of the squall line (denoted by the black box in Figure 9) at 1530 UTC 11 July 2014 for noDA (green line), radarDA (blue line), surfaceDA (red line) and bothDA (orange line) experiments. The dotted lines represent the dew point temperature, and the realizations describe the temperature.

According to the above analysis, it is clear that assimilating surface observation can improve the forecast of the surface temperature and modify the thermodynamic structure within the entire boundary layer, but assimilating radar data has a relatively weak adjustment to the surface temperature and the thermodynamic structure. The assimilation of both radar and surface data can combine the adjustment from both sources to generate a much more reasonable thermodynamic structure within the nocturnal stable boundary layer. From the dew-point result in Figure 11, we can also find that each assimilation experiment increases the dew-point temperature within the boundary layer to some extent.

The three assimilation experiments, with more minor dew-point temperature difference and more significant specific humidity, are more favorable for the evaporative cooling and formation of a stable boundary layer than the noDA experiment.

4.2.2. Dynamic Conditions

Since the boundary layer is stable at night and the wind convergence occurs above the boundary layer, the 800hPa wind and vorticity fields are plotted in Figure 12. The southern side of the black box is dominated by southerly winds with lower speed, and the vorticity inside the box is very weak, resulting in almost no upward movement in the noDA experiment (Figure 12a). After assimilating the observation data, the vorticity on the southwest side of the box is significantly enhanced, and a positive vorticity center is generated at the southwest side of the box (Figure 12b–d). A relatively complete vortex system is formed (Figure 12b), while the surfaceDA experiment does not form a closed vortex system (Figure 12c), and the bothDA experiment generates a complete low vortex system (Figure 12d), which is the southwest vortex described in Section 3.2. This shows that both the radar and surface data assimilation can adjust the circulation patterns to improve the southwest vortex system and significantly enhance the intensity of the southerly winds, which in turn enhances the convergence of the southerly and northerly winds inside the box. To put it specifically, the radarDA experiment and bothDA experiment have stronger vorticity and convergence, while the surfaceDA experiment has relatively weaker vorticity and convergence.

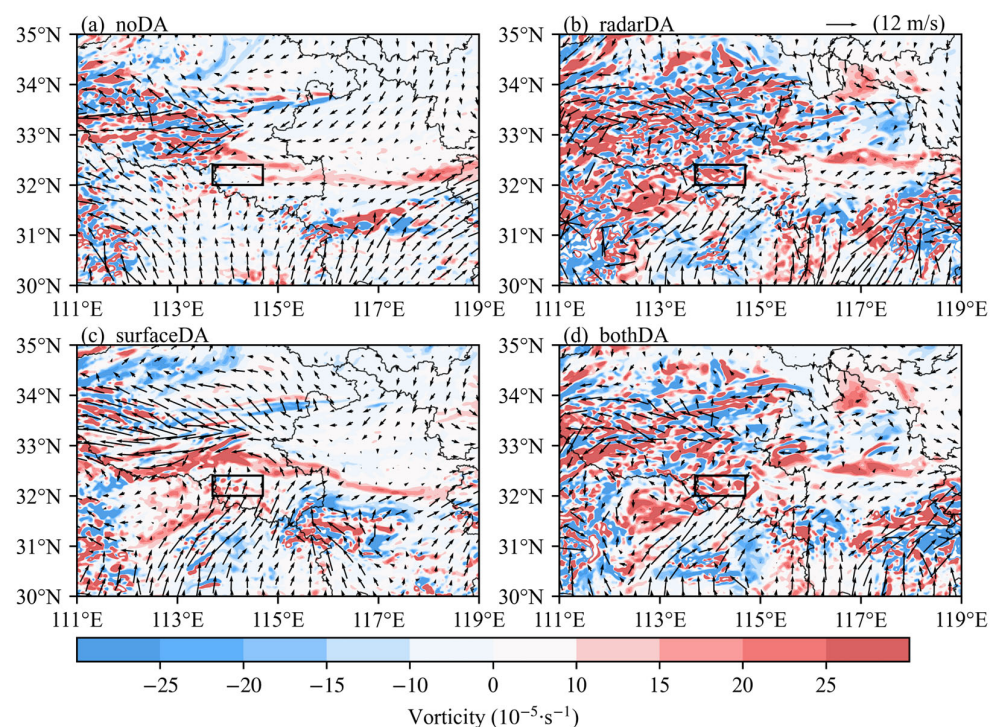


Figure 12. The horizontal distribution of 800 hPa wind fields (quiver, units: m/s) and divergence (shaded, units: $10^{-5} \cdot s^{-1}$) at 1530 UTC 11 July 2014 for (a) noDA, (b) radarDA, (c) surfaceDA and (d) bothDA experiments, the black box in the figure is the same as that in Figure 9.

We analyze the time–height cross sections of area-averaged vertical velocity and divergence further to gain a deeper understanding of the impact of different assimilation experiments on the vertical ascending motion (Figure 13). In terms of the time of convection initiation, the vertical ascending motion appears only after 1630 UTC (Figure 13a) in the noDA experiment. In contrast, all three assimilation experiments generate strong vertical ascending motion between 1530–1630 UTC (Figure 13b–d), which is closer to the time of the squall line formation indicated by the radar reflectivity (Figure 5). From the perspective

of the height of convection, the vertical ascending motion in the radarDA, surfaceDA and bothDA experiments have appeared above 1.5 km from 1530 to 1630 UTC, which predicts the location of the convection initiation above the stable boundary layer accurately (Figure 13b–d). As for the intensity of the vertical ascending motion near the time of convection initiation (1530 UTC) in the radarDA experiment, it is close to $-15 \times 10^{-5} \cdot \text{s}^{-1}$ at the convergence center at the low level, and it is close to $10 \times 10^{-5} \cdot \text{s}^{-1}$ near the divergence center at the high level, resulting in a strong vertical ascending motion between 2–11 km (Figure 13b). Intensities at both the convergence center ($-12 \times 10^{-5} \cdot \text{s}^{-1}$) and divergence center ($5 \times 10^{-5} \cdot \text{s}^{-1}$) in the surfaceDA experiment are weaker than those of the radarDA experiment, and the vertical ascending motion is also weaker, with a lower lifting height of 6 km (Figure 13c). Moreover, the lower layer convergence strength and the vertical convection height in bothDA experiment are equivalent to those in the radarDA experiment, but the divergence center at the higher layer is only about $5 \times 10^{-5} \cdot \text{s}^{-1}$ and the vertical velocity is between the radarDA and surfaceDA experiment (Figure 13d). Combined with the conclusions in Section 4.1, the convection in the radarDA experiment is stronger than the observation, weaker in the surfaceDA experiment than the observation and closer to the observation in the bothDA experiment. It can be seen that the vertical velocity is higher in the radarDA experiment than in the observation, smaller in the surfaceDA experiment and closer to the observation in the both DA experiment.

In summary, both radar and surface data assimilation positively affect the convection initiation time, height and intensity of the squall line. The vertical ascending motion achieved by assimilating radar data is relatively stronger, which in turn leads to stronger convection, while surface data assimilation is weaker, resulting in weaker convection. The reason is related to the difference in spatial coverage between radar and surface data. Assimilating radar data can improve the circulation patterns from low to high level, while the improvement becomes weak with the increase in height in the surface data assimilating. When both radar and surface data are assimilated simultaneously, the forecast is closer to the observation.

4.2.3. Water Vapor Conditions

Figure 14 shows the time–height cross sections of area-averaged specific humidity and the water vapor flux divergence. During the early stage of the squall line formation (1430–1630 UTC), the noDA experiment produces less low-level water vapor (Figure 14a). However, all three assimilation experiments produce apparent water vapor convergence at the low level, with a peak in water vapor flux divergence of about $-25 \times 10^{-5} \cdot \text{s}^{-1}$. Additionally, the specific humidity at the low level is enhanced with a maximum specific humidity larger than $16 \text{ g} \cdot \text{kg}^{-1}$ (Figure 14b–d).

Figure 15 shows the vertical distribution of the area-averaged water vapor and hydrometeor mixing ratios from different experiments. As shown in Figure 15a, the increase in the water vapor mixing ratio (QVAPOR) is largest (about $4 \text{ g} \cdot \text{Kg}^{-1}$) in the radaDA experiment, smallest in the surfaceDA experiment, and in between in the bothDA experiment. At an altitude of 4–9 km, the radarDA and bothDA experiments can also effectively increase QVAPOR. However, the surfaceDA experiment has little influence on it. For the vertical profiles of hydrometeor mixing ratios (Figure 15b–f), the radarDA and bothDA experiments can increase the amount of the rainwater mixing ratio (QRAIN) and cloud water mixing ratio (QCLOUD) up to $0.5 \text{ g} \cdot \text{Kg}^{-1}$ and $0.2 \text{ g} \cdot \text{Kg}^{-1}$ at 0–6 km, respectively, and increase the amount of the graupel mixing ratio (QGRAUP) and snow mixing ratio (QSNOW) up to $0.5 \text{ g} \cdot \text{Kg}^{-1}$ at 5–15 km. However, the surfaceDA experiment has little effect on QRAIN and QCLOUD. All assimilation experiments have a smaller impact on the amount of the ice mixing ratio (QICE) than other hydrometeor mixing ratios.

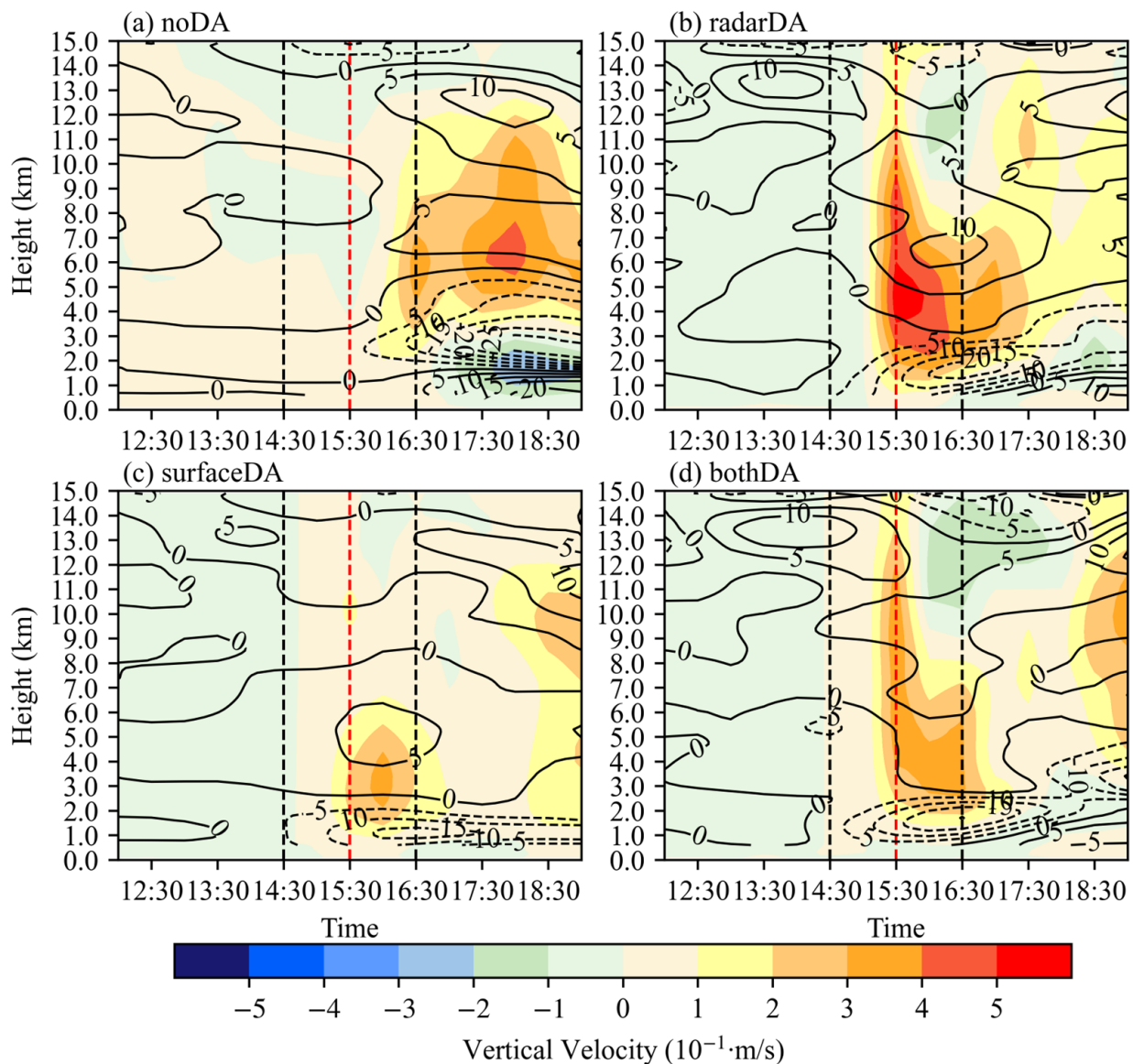


Figure 13. The time–height cross sections of area-averaged vertical velocity (shaded, units: $10^{-1}\cdot\text{m/s}$) and divergence (contour, units: $10^{-5}\cdot\text{s}^{-1}$) from 1200 UTC to 1900 UTC 11 July 2014 for (a) noDA, (b) radarDA, (c) surfaceDA and (d) bothDA experiments. The averaged area is denoted by the black box in Figure 12. The red dotted line represents the time of the squall line initiation, and the two black dotted lines represent the time near the squall line initiation.

It can be concluded that assimilating radar data and surface data can enhance the water vapor conditions in the lower layers, and the improvement is relatively significant in the radar data experiment, resulting in the most favorable water vapor conditions for convection initiation. To put it more precisely, assimilating the radar data significantly increases the water vapor and hydrometeor mixing ratios among the whole troposphere, which may be mainly caused by assimilating the radar reflectivity. In contrast, the surface data assimilation has little effect on the water vapor and hydrometeor mixing ratios. This is also one of the reasons why the radarDA experiment can effectively enhance the intensity of the precipitation, while the surfaceDA experiment has less impact on it.

4.3. Impact on the Forecast of Maintenance of the Squall Line

According to the Rotunno–Klemp–Weisman (RKW) theory [41], the interaction of cold pool and low-level vertical wind shear is one of the important mechanisms for squall

line maintenance. Thus, this section focuses on the impact of different experiments on the forecast of the nocturnal squall line maintenance at the squall line mature stage.

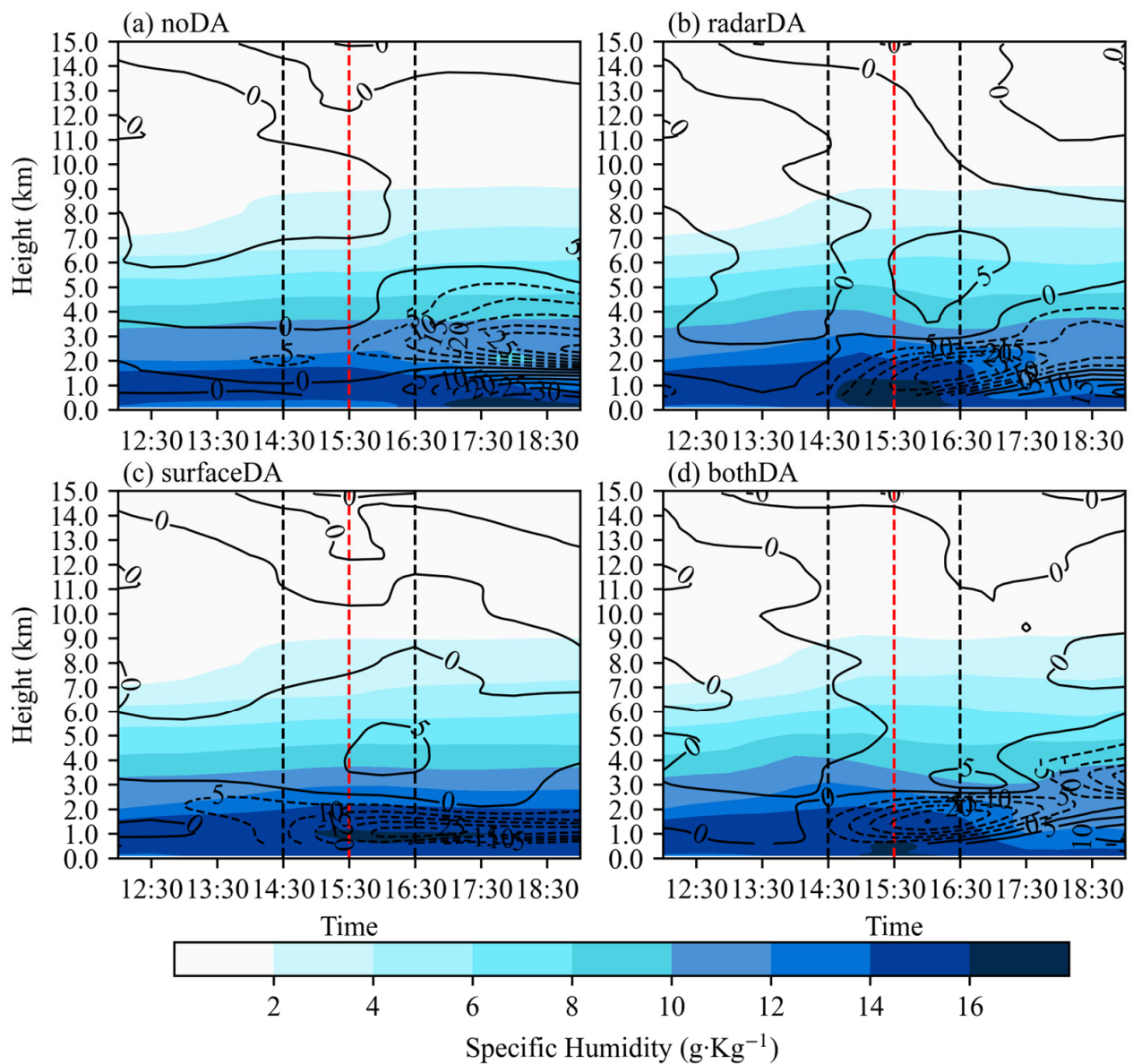


Figure 14. As in Figure 13 but for the specific humidity (shaded, units: $\text{g}\cdot\text{kg}^{-1}$) and the water vapor flux divergence (contour, units: $10^{-5}\cdot\text{s}^{-1}$) for (a) noDA, (b) radarDA, (c) surfaceDA and (d) bothDA experiments.

When the squall line is initiated at 1530 UTC, there is no surface cold pool in the noDA experiment (Figure 16a), while all three assimilation experiments generate surface cold pools (Figure 16b–d). Then, the cold pools in all three assimilation experiments continue to enhance and expand eastward (1700 UTC, Figure 16e–h). During the squall line mature stage (1800 UTC, Figure 16i–l), the noDA experiment generates a weak surface cold pool in southern Henan, while the cold pools of the three assimilation experiments cover the whole southern Henan. Among them, the cold pool of the radarDA and bothDA experiments is stronger than that in the surfaceDA experiment, and the cold pool strength center in the radarDA and bothDA experiments is southward, while the cold pool center is northerly in the surfaceDA experiment. This is mainly related to the position and intensity of the squall lines generated in the three assimilation experiments. The squall line predicted in

the surfaceDA experiment is located in the north with weak intensity, which makes the precipitation position to the north and causes less precipitation, leading to a weak cold pool by precipitation evaporation and a northward center. The position and intensity of the squall line are predicted more accurately in the radarDA and bothDA experiments, resulting in a more accurate center and intensity of the cold pool. It can also be found that the cold pool outflow exists in all three assimilation experiments, and the intensity of the cold pool outflow is related to the cold pool intensity. When the outflow from the cold pool meets with the airflow from the south, it is easy to initiate new convection and then promote the maintenance and development of the squall line.

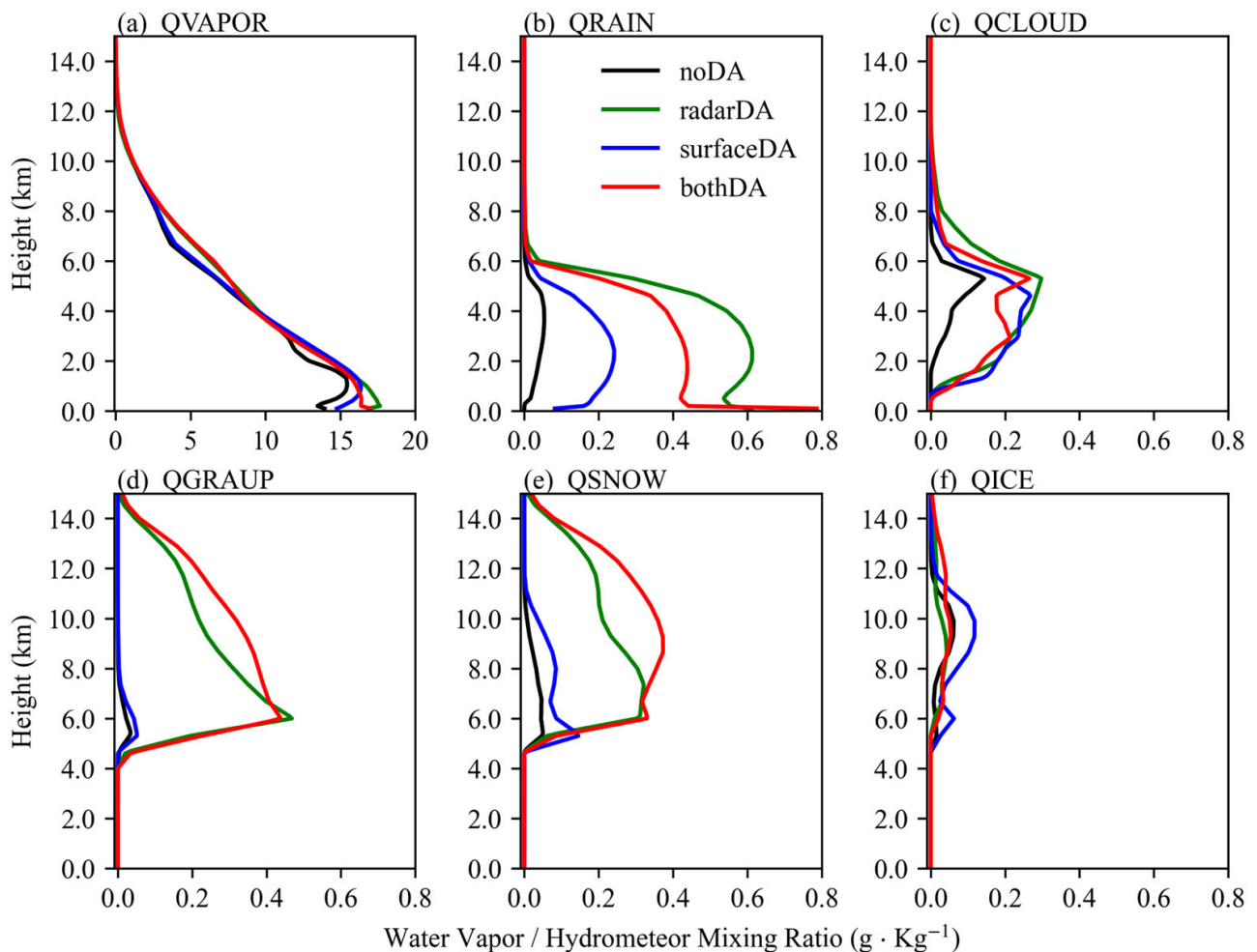


Figure 15. The vertical profiles of the area-averaged (a) water vapor mixing ratio (QVAPOR), (b) rainwater mixing ratio (QRAIN), (c) cloud water mixing ratio (QCLOUD), (d) graupel mixing ratio (QGRAUP), (e) snow mixing ratio (QSNOW), (f) ice mixing ratio (QICE) at 1530 UTC 11 July 2014 for the noDA (black line), radarDA (green line), surfaceDA (blue line) and bothDA (red line) experiments. The black box in Figure 12 denotes the averaged area.

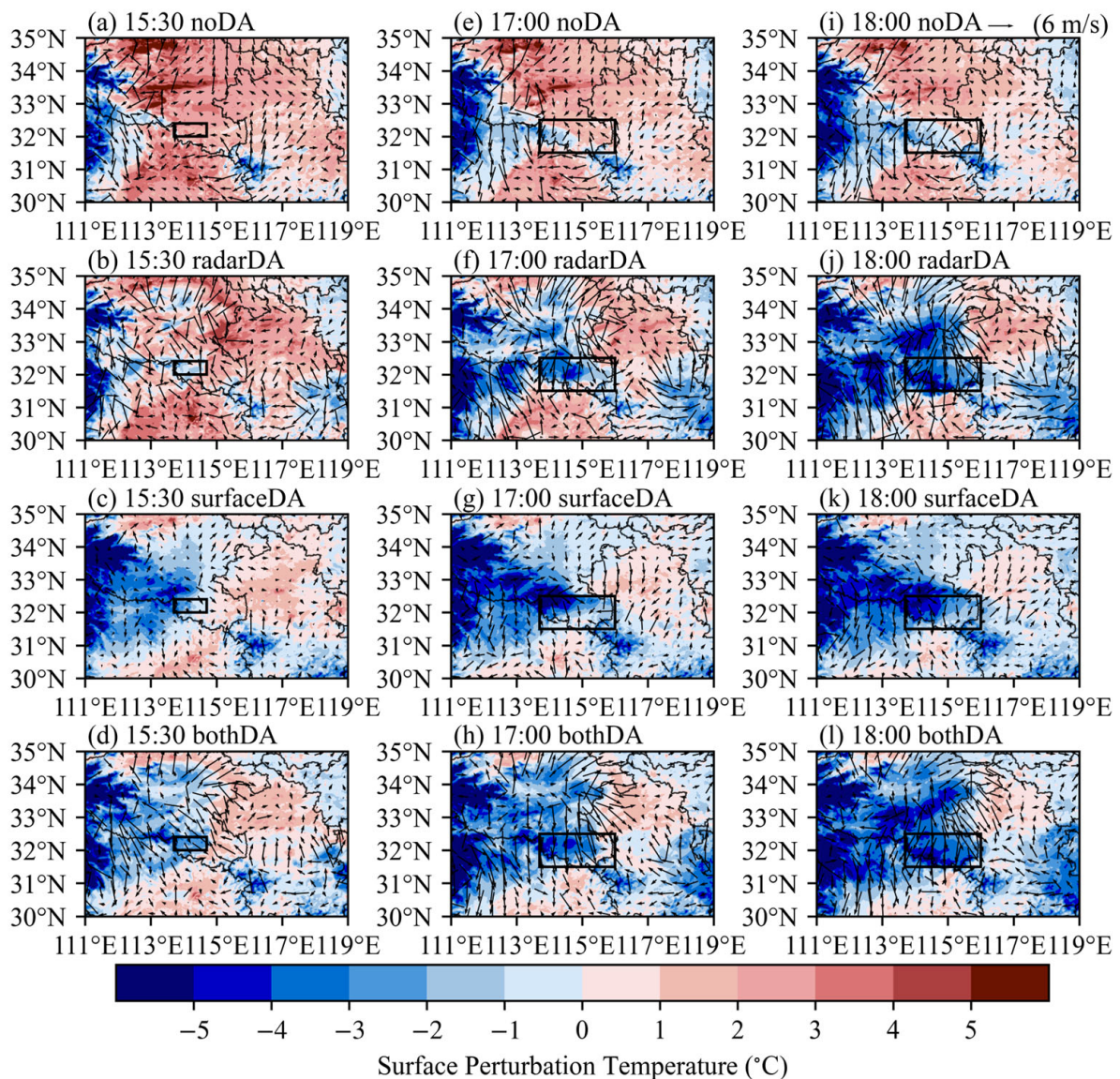


Figure 16. The horizontal distribution of wind field at 10 m (quiver, unit: m/s), and surface perturbation temperature (shaded, unit: °C) at 1530, 1700 and 1800 UTC 11 July 2014 for (a) noDA, (b) radarDA, (c) surfaceDA and (d) bothDA experiments. The black boxes in (a–d) represent the location of initiation of the squall line (same as in Figure 9), and the black boxes in (c–l) represent the location of the main body during the mature of the squall line.

To further analyze the influence of the cold pool and outflow on the maintenance of the squall line, Figure 17 shows the south–north cross sections of in-plane flow vectors and perturbation equivalent potential temperature along 114.6° E at 1800 11 July 2014 for the four experiments. The noDA experiment produces a weak cold center near 32.55° N only near to the surface (Figure 17a). In contrast, a strong cold pool exists in the low troposphere in all three assimilation experiments, and the leading edge of the cold pool reaches near 31.5° N (Figure 17b–d). At the same time, both radarDA and bothDA experiments have strong cold pool outflow north of 31.5° N, and produce strong vertical ascending motion with the generation of new convection near 31° N, promoting development and maintenance of the squall line, while the surfaceDA experiment has weaker outflow at low levels, which has little impact on the development and maintenance of the squall line.

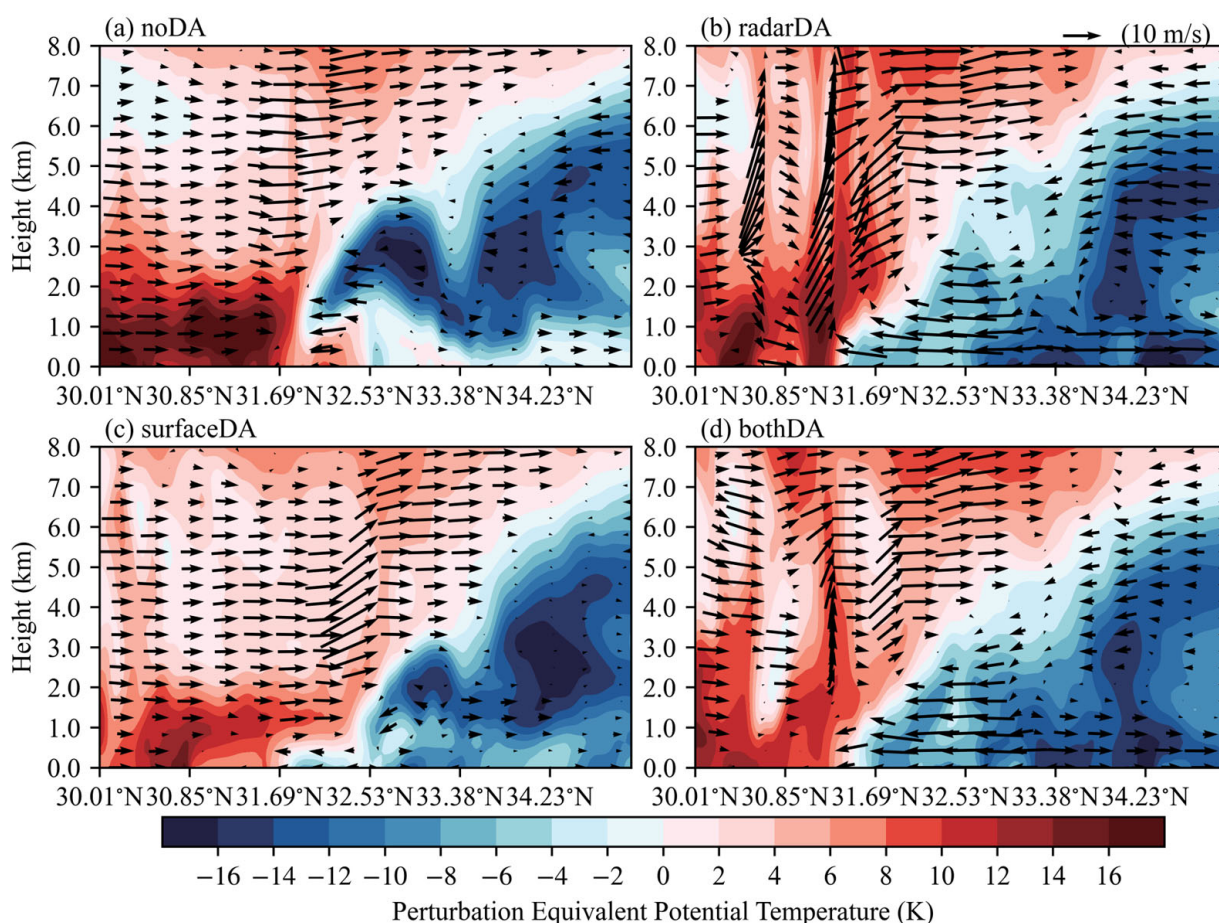


Figure 17. The south–north cross sections of in-plane flow vectors (quiver, units: $\text{m}\cdot\text{s}^{-1}$; vertical motion amplified by a factor of 5) and perturbation equivalent potential temperature (shaded, units: K) along 114.6°E at 1800 UTC 11 July 2014 for (a) noDA, (b) radarDA, (c) surfaceDA and (d) bothDA experiments.

Because of the relatively heavy precipitation predicted by assimilating radar data or both the radar and surface data, a strong cold pool is generated in the precipitation area, and a strong vertical ascending motion is produced near the outflow boundaries. This is more conducive to the development and maintenance of the squall line. However, the precipitation predicted by the assimilation of surface data is weaker, and the cold pool generated is also weaker, which leads to a weak vertical ascending motion and less impact on the development and maintenance of the squall line.

5. Discussion and Conclusions

In this study, the WRF model and WRFDA 3DVar are used to investigate the impact of radar and surface data assimilation on the forecast of a nocturnal squall line in the Yangtze–Huaihe River. The main results and conclusions are as follows:

(1) The assimilation of radar and surface data can improve the forecast skill scores of the reflectivity and precipitation. Radar data assimilation effectively improves the forecasts of both the position and intensity of the reflectivity and precipitation. Surface data assimilation mainly improves the position of reflectivity and precipitation by reducing false radar echoes and precipitation, but it has less impact on the intensity. In addition, assimilating both radar and surface data simultaneously can produce the best forecasts.

(2) During the period of convection initiation, radar data or surface data assimilation can modify the thermodynamic structure of the nocturnal boundary layer. Surface data assimilation reduces the temperature in the near-surface layer, and thus enhances the

stability of the boundary layer. Radar data assimilation has less impact on the near-surface temperature. In addition, radar or surface data assimilation can make more accurate forecasts of the low-level wind field and the southwest vortex, thereby enhancing the convergence of the southerly winds and then improving the forecasts of the time, height and intensity of convection initiation. Radar data assimilation produces stronger vertical ascending motion, leading to stronger convection. On the contrary, surface data assimilation produces weaker vertical ascending motion, resulting in weaker convection. Finally, radar or surface data assimilation can increase the water vapor conditions and hydrometeor mixing ratio, and the enhancement of that in the radar data assimilation is more significant, generating stronger convection.

(3) During the period of maintenance of the nocturnal squall line, radar or surface data assimilation can enhance the evaporative cooling effect, and thereby strengthen the surface cold pool and the outflow. The outflow and the southerly wind converge at the outflow boundary, initiate new convection cells and promote the maintenance and development of the squall line. Moreover, the forecasted precipitation is relatively strong due to the assimilation of radar data or both radar data and surface data, resulting in a strong cold pool and vertical ascending motion, which is more conducive to the maintenance of the squall line. The vertical ascending motion is weaker in the surface data assimilation, which has less impact on the development and maintenance of the squall line.

Compared with the related studies on the severe convection that occurs during the daytime, the assimilation of surface and radar data still has a positive impact on the formation and maintenance of the squall line initiated above the nocturnal stable boundary layer [6,9,10,42]. This study and the related studies also show that the improvement in the skill of precipitation forecasts is most significant when both radar and surface observation data are assimilated simultaneously, whether during the daytime or at night. Johnson et al. (2017) [43] highlighted different roles of assimilating conventional surface observations and radar reflectivity and radial velocity observations: assimilating surface observations mainly improved the mesoscale environment for the radar data assimilation and assimilating radar data improved the systematic forecasts of nocturnal convection. For the nocturnal convection occurring on the Great Plains of the United States, Degelia et al. (2018) [20] showed that the predicting effect of assimilating in situ observations is better than that of assimilating radar observations. They found that assimilating in situ observations improved the forecast of a nocturnal convection initiation event by enhancing the low-level convergence and cold pool generated by the enhanced convection, but assimilating only radar data could not successfully capture convection initiation. However, the effect of assimilating surface data is not as significant as that of assimilating radar data in our study. This may be because we only assimilated surface observations, with no upper-air observations. In addition, the assimilation methods of the two observations also may greatly influence the predicting effect, such as the processing of terrain height in the surface data assimilation and the selection of the reflectivity observation operator in the radar data assimilation. In future research, it is necessary to conduct an in-depth analysis of the differences brought about by the assimilation of the two observations.

Author Contributions: Conceptualization, S.Z.; methodology, S.Z.; software, Z.P.; validation, Z.P.; formal analysis, Z.P.; investigation, Z.P.; resources, Z.P.; data curation, Z.P.; writing—original draft preparation, Z.P.; writing—review and editing, S.Z. and W.Z., funding acquisition, S.Z. All authors have read and agreed to the published version of the manuscript.

Funding: This research was funded by the foundation for National Natural Science Foundation of China (42275088, 41575098) and National Key Research and Development Program of China (2017YFC1502101).

Institutional Review Board Statement: Not applicable.

Informed Consent Statement: Not applicable.

Data Availability Statement: The radar, surface and precipitation data are provided by the “Observation, Prediction and Analysis of severe Convection of China” (OPACC) National “973” Project, the fifth generation ECMWF atmospheric reanalysis of the global climate (ERA5) data on pressure levels can be found at: <https://cds.climate.copernicus.eu/cdsapp#!/dataset/reanalysis-era5-pressure-levels?tab=form> (accessed on 20 February 2022), and the $1^\circ \times 1^\circ$ FNL analysis data from the National Centers for Environment Prediction (NCEP) can be found at <https://rda.ucar.edu/datasets/ds083.2/> (accessed on 30 February 2022).

Acknowledgments: We acknowledge the support of the Supercomputing Center of Lanzhou University.

Conflicts of Interest: The authors declare no conflict of interest.

References

1. Maddox, R.A. Mesoscale convective complexes. *Bull. Am. Meteorol. Soc.* **1980**, *61*, 1374–1387. [[CrossRef](#)]
2. Shou, S.; Li, S.; Yao, X. *Mesoscale Meteorology*; China Meteorological Press: Beijing, China, 2009.
3. Cheng, D.; Shen, T.; Ma, G.; He, D. Advances in the meteorological data assimilation. *J. Nanjing Inst. Meteorol.* **2004**, *27*, 550–564. [[CrossRef](#)]
4. Gao, S.; Min, J.; Huang, D. The simulation of a squall line with doppler radar data assimilation using the ensrf method. *Chin. J. Atmos. Sci.* **2016**, *40*, 1127–1142. [[CrossRef](#)]
5. Zheng, L.; Qiu, X.; Qian, L. Simulation study of a squall line case based on assimilation radar reflectivity data. *Meteorol. Mon.* **2019**, *45*, 73–87. [[CrossRef](#)]
6. Li, S.; Zhang, S.; Zhou, L. Impact of assimilating surface and radar observations on forecasting a squall line with a hybrid data assimilation method: An observation system simulation experiment. *J. Lanzhou Univ. Nat. Sci.* **2020**, *56*, 642–649. [[CrossRef](#)]
7. Shen, F.; Xu, D.; Li, H.; Liu, R. Impact of radar data assimilation on a squall line over the yangtze–huaihe river basin with a radar reflectivity operator accounting for ice-phase hydrometeors. *Meteorol. Appl.* **2021**, *28*, e1967. [[CrossRef](#)]
8. Zhou, W.; Shen, H.; Yuan, H. Impact of radar data assimilation on a squall line. *Chin. J. Atmos. Sci.* **2022**. [[CrossRef](#)]
9. Hou, T.; Kong, F.; Chen, X.; Lei, H. Impact of 3dvar data assimilation on the prediction of heavy rainfall over southern china. *Adv. Meteorol.* **2013**, *2013*, 129642. [[CrossRef](#)]
10. Dong, J.; Xue, M.; Droegemeier, K. The analysis and impact of simulated high-resolution surface observations in addition to radar data for convective storms with an ensemble kalman filter. *Meteorol. Atmos. Phys.* **2011**, *112*, 41–61. [[CrossRef](#)]
11. Cui, X.; Chen, M.; Qin, R.; Han, L. Research advances in the convective initiation mechanisms. *Meteorol. Mon.* **2021**, *47*, 1297–1318. [[CrossRef](#)]
12. Rasmussen, K.L.; Houze, R.A. Convective initiation near the andes in subtropical south america. *Mon. Weather Rev.* **2016**, *144*, 2351–2374. [[CrossRef](#)]
13. Weckwerth, T.M.; Hanesiak, J.; Wilson, J.W.; Trier, S.B.; Degelia, S.K.; Gallus, W.A.; Roberts, R.D.; Wang, X. Nocturnal convection initiation during pecan 2015. *Bull. Am. Meteorol. Soc.* **2019**, *100*, 2223–2239. [[CrossRef](#)]
14. Groff, F.P.; Adams-Selin, R.D.; Schumacher, R.S. Response of MCS low-frequency gravity waves to vertical wind shear and nocturnal thermodynamic environments. *J. Atmospheric Sci.* **2021**, *78*, 3889–3908. [[CrossRef](#)]
15. Bai, H.; Deranadyan, G.; Schumacher, C.; Funk, A.; Epifanio, C.; Ali, A.; Enderwin; Radjab, F.; Adriyanto, R.; Nurhayati, N.; et al. Formation of nocturnal offshore rainfall near the west coast of sumatra: Land breeze or gravity wave? *Mon. Weather Rev.* **2021**, *149*, 715–731. [[CrossRef](#)]
16. Parsons, D.B.; Haghi, K.R.; Halbert, K.T.; Elmer, B.; Wang, J. The potential role of atmospheric bores and gravity waves in the initiation and maintenance of nocturnal convection over the southern great plains. *J. Atmos. Sci.* **2019**, *76*, 43–68. [[CrossRef](#)]
17. Haghi, K.R.; Geerts, B.; Chipilski, H.G.; Johnson, A.; Degelia, S.; Imy, D.; Parsons, D.B.; Adams-Selin, R.D.; Turner, D.D.; Wang, X. Bore-ing into nocturnal convection. *Bull. Am. Meteorol. Soc.* **2019**, *100*, 1103–1121. [[CrossRef](#)]
18. Geerts, B.; Parsons, D.; Ziegler, C.L.; Weckwerth, T.M.; Biggerstaff, M.I.; Clark, R.D.; Coniglio, M.C.; Demoz, B.B.; Ferrare, R.A.; Gallus, W.A.; et al. The 2015 plains elevated convection at night field project. *Bull. Am. Meteorol. Soc.* **2017**, *98*, 767–786. [[CrossRef](#)]
19. Weckwerth, T.M.; Romatschke, U. Where, when, and why did it rain during PECAN? *Mon. Weather Rev.* **2019**, *147*, 3557–3573. [[CrossRef](#)]
20. Degelia, S.K.; Wang, X.; Stensrud, D.J.; Johnson, A. Understanding the impact of radar and in situ observations on the prediction of a nocturnal convection initiation event on 25 june 2013 using an ensemble-based multiscale data assimilation system. *Mon. Weather Rev.* **2018**, *146*, 1837–1859. [[CrossRef](#)]
21. Xue, M. Preface to the special issue on the “observation, prediction and analysis of severe convection of china” (opacc) national “973” project. *Adv. Atmos. Sci.* **2016**, *33*, 1099–1101. [[CrossRef](#)]
22. Helmus, J.; Collis, S. The Python ARM radar toolkit (Py-ART), a library for working with weather radar data in the python programmingl. *J. Open Res. Softw.* **2016**, *4*, e25. [[CrossRef](#)]
23. Bao, X.; Wu, D.; Lei, X.; Ma, L.; Wang, D.; Zhao, K.; Jou, B.J.-D. Improving the extreme rainfall forecast of Typhoon Morakot (2009) by assimilating radar data from Taiwan Island and mainland China. *J. Meteorol. Res.* **2017**, *31*, 747–766. [[CrossRef](#)]
24. Jiyang, T.; Ronghua, L.; Liuqian, D.; Liang, G.; Bingyu, Z. Typhoon rainstorm simulations with radar data assimilation on the southeast coast of China. *Nat. Hazards Earth Syst. Sci.* **2021**, *21*, 723–742. [[CrossRef](#)]

25. Lin, E.; Yang, Y.; Qiu, X.; Xie, Q.; Gan, R.; Zhang, B.; Liu, X. Impacts of the radar data assimilation frequency and large-scale constraint on the short-term precipitation forecast of a severe convection case. *Atmos. Res.* **2021**, *257*, 105590. [[CrossRef](#)]
26. Skamarock, C.; Klemp, B.; Dudhia, J.; Gill, O.; Liu, Z.; Berner, J.; Wang, W.; Powers, G.; Duda, G.; Barker, D.; et al. *A Description of the Advanced Research WRF Model Version 4.3*; NCAR: Boulder, CO, USA, 2021. [[CrossRef](#)]
27. Parrish, D.F.; Derber, J.C. The national meteorological center's spectral statistical-interpolation analysis system. *Mon. Weather Rev.* **1992**, *120*, 1747–1763. [[CrossRef](#)]
28. Sun, J.; Wang, H.; Tong, W.; Zhang, Y.; Lin, C.-Y.; Xu, D. Comparison of the impacts of momentum control variables on high-resolution variational data assimilation and precipitation forecasting. *Mon. Weather Rev.* **2016**, *144*, 149–169. [[CrossRef](#)]
29. Li, X.; Zeng, M.; Wang, Y.; Wang, W.; Wu, H.; Mei, H. Evaluation of two momentum control variable schemes and their impact on the variational assimilation of radarwind data: Case study of a squall line. *Adv. Atmos. Sci.* **2016**, *33*, 1143–1157. [[CrossRef](#)]
30. Shen, F.; Min, J.; Li, H.; Xu, D.; Shu, A.; Zhai, D.; Guo, Y.; Song, L. Applications of radar data assimilation with hydrometeor control variables within the wrfda on the prediction of landfalling hurricane ike (2008). *Atmosphere* **2021**, *12*, 853. [[CrossRef](#)]
31. Sun, J.; Crook, N.A. Dynamical and microphysical retrieval from doppler radar observations using a cloud model and its adjoint. Part I: Model development and dimulated data experiments. *J. Atmos. Sci.* **1997**, *54*, 1642–1661. [[CrossRef](#)]
32. Tong, M.; Xue, M. Ensemble kalman filter assimilation of doppler radar data with a compressible nonhydrostatic model: OSS experiments. *Mon. Weather Rev.* **2005**, *133*, 1789–1807. [[CrossRef](#)]
33. Ruggiero, F.H.; Sashegyi, K.D.; Madala, R.V.; Raman, S. The use of surface observations in four-dimensional data assimilation using a mesoscale model. *Mon. Weather Rev.* **1996**, *124*, 1018–1033. [[CrossRef](#)]
34. Hong, S.-Y.; Noh, Y.; Dudhia, J. A new vertical diffusion package with an explicit treatment of entrainment processes. *Mon. Weather Rev.* **2006**, *134*, 2318–2341. [[CrossRef](#)]
35. Lim, K.-S.S.; Hong, S.-Y. Development of an effective double-moment cloud microphysics scheme with prognostic cloud condensation nuclei (ccn) for weather and climate models. *Mon. Weather Rev.* **2010**, *138*, 1587–1612. [[CrossRef](#)]
36. Mlawer, E.J.; Taubman, S.J.; Brown, P.D.; Iacono, M.J.; Clough, S.A. Radiative transfer for inhomogeneous atmospheres: RRTM, a validated correlated-k model for the longwave. *J. Geophys. Res. Atmos.* **1997**, *102*, 16663–16682. [[CrossRef](#)]
37. Dudhia, J. Numerical study of convection observed during the winter monsoon experiment using a mesoscale two-dimensional model. *J. Atmos. Sci.* **1989**, *46*, 3077–3107. [[CrossRef](#)]
38. Fei, C.; Jimmy, D. Coupling an advanced land surface-hydrology model with the penn state-ncar mm5 modeling system. part i: Model implementation and sensitivity. *Mon. Weather Rev.* **2001**, *129*, 17.
39. Kain, J.S.; Fritsch, J.M. Convective Parameterization for Mesoscale Models: The Kain-Fritsch Scheme. In *The Representation of Cumulus Convection in Numerical Models*; Emanuel, K.A., Raymond, D.J., Eds.; Meteorological Monographs; American Meteorological Society: Boston, MA, USA, 1993; pp. 165–170. ISBN 978-1-935704-13-3.
40. He, Z.; Zhang, Q.; Zhao, K.; Hu, H. Initiation and evolution of elevated convection in a nocturnal squall line along the meiyu front. *J. Geophys. Res. Atmos.* **2018**, *123*, 7292–7310. [[CrossRef](#)]
41. Rotunno, R.; Klemp, J.B.; Weisman, M.L. A theory for strong, long-lived squall lines. *J. Atmos. Sci.* **1988**, *45*, 463–485. [[CrossRef](#)]
42. Chen, I.-H.; Hong, J.-S.; Tsai, Y.-T.; Fong, C.-T. Improving afternoon thunderstorm prediction over Taiwan through 3DVar-based radar and surface data assimilation. *Weather Forecast.* **2020**, *35*, 2603–2620. [[CrossRef](#)]
43. Johnson, A.; Wang, X.; Degelia, S. Design and implementation of a gsi-based convection-allowing ensemble-based data assimilation and forecast system for the pecan field experiment. part ii: Overview and evaluation of a real-time system. *Weather Forecast.* **2017**, *32*, 1227–1251. [[CrossRef](#)]